POLITECNICO DI MILANO
Scuola di Ingegneria Industriale e dell'Informazione
Laurea magistrale in Ingegneria Matematica

3D Transient Drift-Diffusion Simulation of Semiconductor Devices in Presence of Impact Ionization

Relatore: Prof. Riccardo SACCO
Correlatore: Dott. Aurelio Giancarlo MAURI

Tesi di Laurea di:
Claudio Tribbia
Matr. n. 801783

Anno Accademico 2015–2016

a Daniele

Indice

Elenco delle figure

Elenco delle tabelle

Estratto della tesi

Nel 1959, presso i Laboratori Bell, Dawon Kahng e Martin Atalla realizzarono il primo transistor metallo-ossido-semiconduttore a effetto di campo (MOSFET). Dieci anni più tardi, i ricercatori Don Scharfetter e Hermann Gummel, pubblicarono un articolo diventato una pietra miliare nella letteratura della simulazione numerica dei dispositivi a semiconduttore [8]. Da allora, il mondo dell'elettronica ha subìto un'evoluzione rapidissima, producendo e commercializzando dispositivi sempre più piccoli e veloci ad ogni generazione: svariati miliardi di transistori vengono integrati in pochi centimetri quadrati e ognuno di essi è caratterizzato da una lunghezza di canale di una quindicina di nanometri.

In tale contesto, i progressi effettuati nel campo della simulazione numerica acquisiscono una rilevanza fondamentale: da un punto di vista economico, la capacità di prevedere il comportamento di un dispositivo prima della sua effettiva realizzazione porta enormi benefici, dati gli elevatissimi costi di produzione dei prototipi. Allo stesso tempo, la possibilità di ottenere informazioni di carattere quantitativo senza la necessità di effettuare misure è estremamente preziosa in fase di progettazione.

Il lavoro svolto nell'ambito di questa tesi è stato dedicato all'estensione di FEMOS-MP (*Finite Element Method Oriented Solver - MultiPhysics*) con moduli relativi alla simulazione dei semiconduttori, migliorandone le prestazioni e aumentando l'integrazione della struttura del codice. Ciò ha permesso di introdurre gli schemi di discretizzazione temporale Backward Euler e TRBDF2 [2] per la simulazione in transitorio del modello Drift-Diffusion. Inoltre sono state gettate le fondamenta per la simulazione in temperatura, in vista di un futuro accoppiamento con un opportuno modello termico. La bontà dell'implementazione è stata poi validata conducendo svariate simulazioni e confrontandone i risultati con quelli ottenuti da un codice commerciale.

L'elaborato è organizzato come segue:

Capitolo 1 contiene una sintetica, ma rigorosa, trattazione matematica del trasporto di carica nei semiconduttori: la presentazione dell'approccio Drift-Diffusion viene arricchita dalla descrizione e modellizzazione dei fenomeni di generazione/ricombinazione e di degradazione della mobilità dei portatori.

Capitolo 2 vengono illustrate le tecniche numeriche utilizzate per la risoluzione del sistema di equazioni a derivate parziali che costituiscono il modello: le prime due sezioni sono dedicate al problema stazionario, mentre l'ultima affronta la discretizzazione del modello tempo-dipendente, descrivendo gli schemi temporali utilizzati.

Capitolo 3 sono presentati i risultati relativi alle simulazioni del modello Drift-Diffusion stazionario per due strutture MOSFET, una di tipo n e una di tipo p, e comprende l'analisi dei dispositivi in polarizzazione diretta -con approfondimenti riguardanti l'importanza dei vari modelli di mobilità, l'effetto body, la dipendenza dalla temperatura- e lo studio in regime di polarizzazione inversa.

Capitolo 4 riporta i risultati ottenuti dalle simulazioni del modello tempo dipendente per differenti impulsi di polarizzazione.

Capitolo 5 vengono tratte le conclusioni sul lavoro svolto e suggeriti i possibili sviluppi futuri.

Introduction

In 1959, at Bell Labs, Dawon Kahng and Martin Atalla realized the first metal-oxide-semiconductor field-effect transistor (MOSFET). Ten years later, the researchers Don Scharfetter and Hermann Gummel published an article that has become a milestone in the literature numerical simulation for semiconductor devices [8]. Since then, the world of electronics has undergone a tremendously rapid evolution, manufacturing and commercializing devices which are smaller and faster at each new generation: billions of transistors are embedded in a few squared centimeters, each of them being characterized by a channel length of about fifteen nanometers.

In such a context, the progress made in numerical simulation acquires a fundamental relevance: from an economical point of view, the ability to predict a device behaviour prior to its construction brings great benefits, given the high production costs of early prototypes. At the same time, the possibility of obtaining quantitative information without the need of performing measurements is extremely valuable during the design phase.

The work done in this thesis has been devoted to the extension of FEMOS-MP (*Finite Element Method Oriented Solver - MultiPhysics*) with modules related to semiconductor simulation, by improving performance and enhancing the code framework integration. These efforts have made possible the introduction of the Backward Euler and TRBDF2 time discretization schemes for enabling the transient simulation of the Drift-Diffusion model. Moreover, we have layed the foundations for the temperature dependent simulation, in view of the coupling of the Drift-Diffusion model with a proper thermal model.

The thesis is organized as follows:

Chapter 1 provides a synthetic, still rigorous, mathematical model of charge transport in semiconductor materials: the Drift-Diffusion ap-

proach is theoretically obtained and enriched with the description and modeling of generation/recombination and carrier mobilities degradation phenomena.

Chapter 2 discusses the numerical techniques employed for solving the system of partial differential equations constituting the model: the first two sections are dedicated to the discretization of the stationary problems, whereas the latter one is devoted to the discretization of the time-dependent model.

Chapter 3 reports the simulation results in the case of the stationary Drift-Diffusion model for a n-channel and a p-channel MOSFET: we analyze these devices in forward bias conditions - with deepenings regarding mobility models, the body effect, the temperature dependence- and in reverse bias regime.

Chapter 4 illustrates the simulation results obtained by solving the time-dependent Drift-Diffusion model with different bias pulses.

Chapter 5 presents our conclusions and suggestions for possible future works.

Sommario

In questa tesi ci siamo dedicati alla simulazione di dispositivi a semiconduttore nell'ambito dello sviluppo del codice FEMOS-MP. Abbiamo esteso il codice includendo modelli per nuovi fenomeni fisici (band-to-band tunneling, riduzione del bandgap, degradazione della mobilità indotta dal campo elettrico) e implementando schemi di avanzamento temporale per le simulazioni in transitorio.

La procedura adottata per risolvere il modello Drift-Diffusion sfrutta l'algoritmo della mappa di Gummel per disaccoppiare il sistema, dopodiché l'equazione di Poisson viene risolta applicando il metodo di Newton e una discretizzazione a elementi finiti lineari, mentre per le equazioni di continuità viene utilizzato il metodo EAFE. Per quanto riguarda le simulazioni in transitorio, la derivata temporale è stata discretizzata utilizzando gli schemi Backward Euler e TRBDF2.

Per verificare la correttezza dell'implementazione diversi test sono stati effettuati su una struttura MOSFET: per il caso stazionario viene condotta un'analisi in regime di polarizzazione diretta ed inversa, con approfondimenti riguardanti la modellizzazione della mobilità, l'effetto body e la dipendenza dalla temperatura, mentre le simulazioni in transitorio sono state effettuate utilizzando svariati impulsi di polarizzazione.

Abstract

In this thesis, we have addressed the 3D simulation of semiconductor devices within the framework of the FEMOS-MP computer code.

We have extended the code by embedding models for additional physical phenomena (band-to-band tunneling R/G mechanism, bandgap narrowing, mobility degradation induced by the electric field) and including time discretization schemes for transient simulations.

The procedure adopted for solving the Drift-Diffusion model exploits the Gummel map algorithm to decouple the system, after that the Nonlinear Poisson equation is solved by applying the Newton method and a linear finite element discretization, while for the continuity equations the EAFE scheme is employed. As regards the transient simulations the time derivative is discretized using either the Backward Euler or the TRBDF2 method.

To assess the correct implementation of model and numerical methods, several tests have been performed on a MOSFET structure: a stationary analysis has been provided in both forward and reverse bias regimes, with deepenings regarding the moblity modeling, the body-effect and the temperature dependence, while transient simulations have been conducted for a wide variety of bias pulses.

Chapter 1

Mathematical Models for Semiconductors

The numerical simulation of seiconductor devices is based on the *Drift-Diffusion* model, an incomplete parabolic nonlinear system of PDEs. In this chapter we will describe in detail the Drift-Diffusion system and the assumptions underlying its derivation. For further information we refer to [9], [18] and [12].

1.1 The Drift Diffusion Model

The Drift-Diffusion model (DD) is made by three equations describing the carrier conservation and the electrostatic potential distribution in the semiconductor device. The DD model can be derived from Maxwell's equations which are usually written as [9]:

$$\nabla \cdot \mathbf{D} = \rho \tag{1.1}$$

$$\nabla \cdot \mathbf{B} = 0 \tag{1.2}$$

$$\nabla \times \mathbf{E} = \frac{\partial \mathbf{D}}{\partial t} \tag{1.3}$$

$$\nabla \times \mathbf{H} = \mathbf{J} + \frac{\partial \mathbf{D}}{\partial t} \tag{1.4}$$

having indicated by t the time variable [s], by ρ the space charge density [$\mathrm{C\,m^{-3}}$], by $\mathbf{E}$ the electric field [$\mathrm{V\,m^{-1}}$], by $\mathbf{B}$ the magnetic field [$\mathrm{N\,m^{-1}\,A^{-1}}$] and where $\mathbf{J}$ is the current density [$\mathrm{A\,m^{-2}}$], while $\mathbf{D}$ and $\mathbf{H}$ are the displacement field [$\mathrm{C\,m^{-2}}$] and the magnetizing field [$\mathrm{A\,m^{-1}}$], respectively, and satisfy

the following *constitutive laws*:

$$\mathbf{D} = \varepsilon \mathbf{E} \tag{1.5}$$

$$\mathbf{B} = \mu \mathbf{H} \tag{1.6}$$

with ε and μ being the electric permittivity [$\mathrm{F\,m^{-1}}$] and magnetic permeability [$\mathrm{H\,m^{-1}}$] of the considered medium, respectively. Exploiting the solenoidality of the magnetic field, a vector potential $\mathbf{A}$ can be determined in a such way that

$$\nabla \times \mathbf{A} = \mathbf{B}\,. \tag{1.7}$$

Replacing (1.7) in Maxwell-Faraday's law (1.3), we have

$$\nabla \times \left(\mathbf{E} + \frac{\partial \mathbf{A}}{\partial t} \right) = \mathbf{0}\,. \tag{1.8}$$

Relation (1.8) implies that there exists a scalar function φ such that

$$\mathbf{E} + \frac{\partial \mathbf{A}}{\partial t} = -\nabla \varphi\ . \tag{1.9}$$

It is important to notice that the choice of $\mathbf{A}$ and φ is not unique, in fact, given a regular scalar function $\psi = \psi(\mathbf{x}, t)$, the following expressions

$$\mathbf{A}' = \mathbf{A} + \nabla \psi \qquad \text{and} \qquad \varphi' = \varphi - \frac{\partial \psi}{\partial t} \tag{1.10}$$

can replace their original counterparts. Multiplying (1.9) by ε and applying the divergence operator we get

$$\nabla \cdot \left(\mathbf{D} + \varepsilon \frac{\partial \mathbf{A}}{\partial t} \right) = -\nabla \cdot (\varepsilon \nabla \varphi) \tag{1.11}$$

so that, using (1.1), we have

$$-\varepsilon \frac{\partial \nabla \cdot \mathbf{A}}{\partial t} - \nabla \cdot (\varepsilon \nabla \varphi) = \rho. \tag{1.12}$$

Exploiting the degree of freedom on the choice of $\mathbf{A}$, we impose the Coulomb gauge-fixing condition $\nabla \cdot \mathbf{A} = 0$, so that the Poisson equation for the electrostatic potential φ can be finally obtained from (1.12):

$$-\nabla \cdot (\varepsilon \nabla \varphi) = \rho. \tag{1.13}$$

The charge density distribution can be subdivided as:

$$\rho = q(p - n) + q(N_D^+ - N_A^-) \tag{1.14}$$

where q is the electron charge ($q = 1.602 \times 10^{-19}$ [C]), n, p are the mobile electron and hole densities, while N_D^+, N_A^- are the effective donor and acceptor concentrations. These latter are fixed time invariant concentrations not necessarily uniform in space.

To derive the carrier continuity equations, we fix an arbitrary control volume V of boundary ∂V, centered at a point $\mathbf{x}$ and write the following balance holding for the charge density ρ:

$$\frac{\partial}{\partial t}\int_V \rho \, dV + \int_{\partial V} \mathbf{J}\cdot\mathbf{n} \, d\sigma = 0. \tag{1.15}$$

where $\mathbf{n}$ is the outward unit normal vector on ∂V. Thanks to Gauss theorem and due to the arbitrary choice of V, we have the differential form of the continuity equation (1.15):

$$\frac{\partial \rho}{\partial t} + \nabla\cdot\mathbf{J} = 0\,. \tag{1.16}$$

The total current density can be splitted by considering separately the electron and hole contributions:

$$\mathbf{J}^{drift} = \mathbf{J}_n + \mathbf{J}_p\,. \tag{1.17}$$

Replacing (1.14) and (1.17) in (1.16) we can decompose the continuity equation in two distinct relationships:

$$-q\frac{\partial n}{\partial t} + \nabla\cdot\mathbf{J}_n = qR \tag{1.18}$$

$$q\frac{\partial p}{\partial t} + \nabla\cdot\mathbf{J}_p = -qR \tag{1.19}$$

where we have introduced the scalar function $R = R(\mathbf{x}, t)$ which represents the carrier net generation/recombination rate [$\mathrm{m}^{-3}\,\mathrm{s}^{-1}$] and will be discussed in detail in Sect. 1.3.2.

Current densities $\mathbf{J}_n$ and $\mathbf{J}_p$ can be viewed as the result of two different terms:

- the *drift* component, which considers the motion of carriers subject to the electric field;
- the *diffusion* component, that takes into account the spontaneous tendancy of carriers to spread from regions with high concentration towards regions with a lower one.

Using the semi-classical approach (*Drude model*), a carrier subjected to an electric field has an average velocity given by:

$$\mathbf{v}_n = -\frac{q\tau_n \mathbf{E}}{m_e^*}\,, \qquad \mathbf{v}_p = \frac{q\tau_p \mathbf{E}}{m_h^*}$$

where τ_n, τ_p are the momentum relaxation times for electrons and holes [s] and are related to the *scattering* that occurs between the carriers and the other atoms nearby, while m_e^* and m_h^* [kg] are the conduction equivalent masses depending on the *energy-momentum relationship* which characterizes the band structure of the particular medium. Introducing the electron and hole mobilities $[\mathrm{m^2\,s^{-1}\,V^{-1}}]$

$$\mu_n = \frac{q\tau_n}{m_n^*}\,, \tag{1.20}$$

$$\mu_p = \frac{q\tau_p}{m_p^*}\,, \tag{1.21}$$

it is possible to calculate the drift current densities as:

$$\mathbf{J}_n^{drift} = -qn\mathbf{v}_n = qn\mu_n\mathbf{E}\,, \tag{1.22}$$

$$\mathbf{J}_p^{drift} = +qp\mathbf{v}_p = qp\mu_p\mathbf{E}\,. \tag{1.23}$$

By adding together (1.22) and (1.23) the well-known *Ohm's law* can be obtained:

$$\mathbf{J} = \mathbf{J}_n^{drift} + \mathbf{J}_p^{drift} = q(n\mu_n + p\mu_p)\mathbf{E} = \sigma\mathbf{E} \tag{1.24}$$

where σ is the total electric conductivity [S] of the electron and hole gas.
The diffusion current term can be otained using *Fick's law of diffusion* as:

$$\mathbf{J}_n^{diff} = -D_n\nabla(-qn)\,, \tag{1.25}$$

$$\mathbf{J}_p^{diff} = -D_p\nabla(+qp) \tag{1.26}$$

where D_n and D_p are the electron and hole diffusivity coefficients $[\mathrm{m^2\,s^{-1}}]$. Combining equations (1.22)-(1.23) with (1.25)-(1.26) we obtain the following expressions for $\mathbf{J}_n$ and $\mathbf{J}_p$:

$$\mathbf{J}_n = qn\mu_n\mathbf{E} + qD_n\nabla n\,, \tag{1.27}$$

$$\mathbf{J}_p = qp\mu_p\mathbf{E} - qD_p\nabla p\,. \tag{1.28}$$

Therefore, collecting (1.1), (1.14), (1.18), (1.19), (1.5), (1.27), (1.28), we

obtain the *Drift-Diffusion model* for semiconductors:

$$\begin{cases} \nabla \cdot \mathbf{D} = q(p-n) + q(N_D^+ - N_A^-) \\ -q\dfrac{\partial n}{\partial t} + \nabla \cdot \mathbf{J}_n = qR \\ q\dfrac{\partial p}{\partial t} + \nabla \cdot \mathbf{J}_p = -qR \\ \mathbf{D} = \varepsilon \mathbf{E} = -\varepsilon \nabla \varphi \\ \mathbf{J}_n = qn\mu_n \mathbf{E} + qD_n \nabla n \\ \mathbf{J}_p = qp\mu_p \mathbf{E} - qD_p \nabla p \quad . \end{cases} \tag{1.29}$$

The above set of equations is an *incomplete parabolic nonlinear* system in the dependent variables $\varphi = \varphi(\mathbf{x}, t)$, $n = n(\mathbf{x}, t)$ and $p = p(\mathbf{x}, t)$.

1.2 Geometry, Boundary and Initial Conditions

Let us consider Fig. 1.1 which depicts the 3D geometry of a MOSFET that is commonly employed in industrial numerical simulation. The computational domain, Ω, is the union of two disjoints open sets Ω_{Si} and Ω_{ox} representing the silicon and oxide region, respectively. The oxide portion is assumed to be a perfect insulator, therefore no mobile charge is present in its volume and no electric current can flow throughout it:

$$\begin{cases} n = p = 0 \\ \mathbf{J}_n = \mathbf{J}_p = \mathbf{0}. \end{cases} \qquad \text{in } \Omega_{ox} \tag{1.30}$$

The entire domain boundary, $\partial\Omega$, is divided in two different subsets: $\partial\Omega_a$ and $\partial\Omega_c$. The set $\partial\Omega_c$ includes the Ohmic contacts on the transistor -namely the gate, drain, source and bulk contacts- while the set $\partial\Omega_a$ is the artificial boundary and includes the remaining boundary parts, $\partial\Omega_a = \partial\Omega \setminus \partial\Omega_c$. Ohmic contacts are assumed ideal, i.e. they are equipotential surfaces at which no voltage drops occur, thus they can be treated with Dirichlet conditions for the variables φ, n and p:

$$\begin{cases} \varphi = \varphi_D \\ n = n_D \\ p = p_D \end{cases} \qquad \text{on } \Gamma_D \tag{1.31}$$

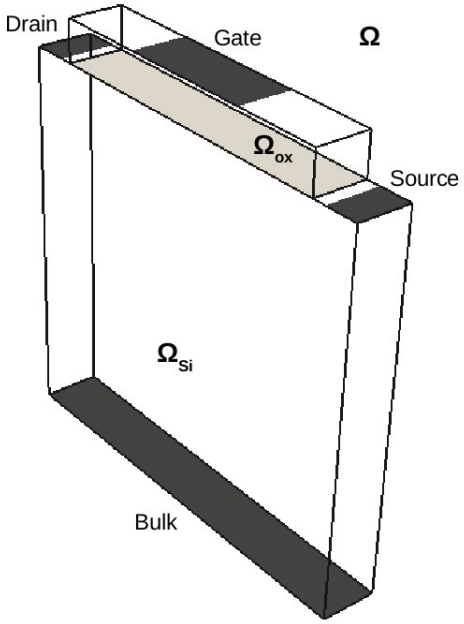

Figure 1.1: 3D geometry of a MOSFET

having set $\Gamma_D = \Omega_c$. To determine φ_D, n_D and p_D we enforce thermodynamical equilibrium and charge neutrality that correspond to the following system valid on Γ_D:

$$\begin{cases} np - n_i^2 = 0 & \text{(1.32a)} \\ p_D - n_D + D = 0 & \text{(1.32b)} \end{cases}$$

where D is the net doping concentration defined as $D(\mathbf{x}) = N_D^+(\mathbf{x}) - N_A^-(\mathbf{x})$ whereas n_i is the intrinsic carrier concentration of the semiconductor material. Solving for n_D and p_D yields:

$$n_D = \frac{D + \sqrt{D^2 + 4n_i^2}}{2}\,, \tag{1.33}$$

$$p_D = \frac{-D + \sqrt{D^2 + 4n_i^2}}{2}\,. \tag{1.34}$$

It is important to point out that, from a numerical standpoint formulae (1.33) and (1.34) should not be used directly in all cases: in fact, the doping is typically orders of magnitude greater than the intrinsic concentration and this may likely cause cancellation errors when resolving the outer algebraic sum. A safer approach is to perform the computation on the equation having the first term positive (so that it will be summed together with the result

of the square root) and calculating the other using the law of mass action (1.32a). For example, in a p-type region the datum p_D is determined from (1.34) while the minority carrier density n_D is computed using (1.32a) and obtaining $n_D = n_i^2/p_D$.
Before computing the datum φ_D, let us introduce the Maxwell-Boltzmann statistics for the electron and hole densities:

$$n = n_i e^{\frac{\varphi - \varphi_n}{V_{th}}}, \tag{1.35}$$

$$p = n_i e^{\frac{\varphi_p - \varphi}{V_{th}}}, \tag{1.36}$$

where $V_{th} = k_B T/q$ is the thermal voltage, k_B and T denoting the Boltzmann constant ($k_B = 1.3806\,\mathrm{m^2 kgs^{-2}K^{-1}}$) and the absolute temperature [K], respectively, and having denoted by φ_n and φ_p the electron and hole quasi Fermi potentials, respectively.
The condition that has to be imposed on the electrostatic potential can be recovered using the equilibrium local assumption, according to which that Fermi potential φ_f is unique and equal to the externally applied voltage V_{ext}:

$$\varphi_n = \varphi_p = \varphi_f = V_{ext}\,. \tag{1.37}$$

Then, the boundary value for the electrostatic potential potential φ_D can be easily calculated exploiting relation (1.37) in (1.35) and (1.36):

$$\varphi_D = V_{ext} + V_{th} \ln\left(\frac{n_D}{n_i}\right) = V_{ext} - V_{th} \ln\left(\frac{p_D}{n_i}\right)\,. \tag{1.38}$$

The treatment of the artifical boundary, $\partial\Omega_a$, follows from the need of performing a self-contained simulation and prescribes no flux exchange with the outer environment (homogeneous Neumann conditions):

$$\begin{cases} \mathbf{D}\cdot\mathbf{n} = 0 \\ \mathbf{J}_n\cdot\mathbf{n} = 0 \\ \mathbf{J}_p\cdot\mathbf{n} = 0 \end{cases} \qquad \text{on } \Gamma_N \tag{1.39}$$

where we have set $\Gamma_N = \partial\Omega_a$. Given (1.30), the carrier continuity equations have to be solved in the silicon domain only, thus the boundaries become:

$$\Gamma_{D,Si} = \Gamma_D \cap \partial\Omega_{Si}$$
$$\Gamma_{N,Si} = \Gamma_N \cap \partial\Omega_{Si} \cup \Gamma_{int}$$

$\Gamma_{int} = \partial\Omega_{Si} \cap \partial\Omega_{ox}$ denoting the interface between oxide and silicon. On these sets the same boundary conditions for Γ_D and Γ_N have to be applied (i.e., (1.31) and (1.39)). Mathematically writing the Drift-Diffusion model for the MOSFET structure, we end up with the following initial value/boundary value system of equations:

$$\nabla \cdot (-\varepsilon \nabla \varphi) - q(p - n) - q(N_D^+ - N_A^-) = 0 \qquad \text{in } \Omega \tag{1.40}$$
$$\varphi = \varphi_D \qquad \text{on } \Gamma_D \tag{1.41}$$
$$\nabla \varphi \cdot \mathbf{n} = 0 \qquad \text{on } \Gamma_N \tag{1.42}$$

$$-q\frac{\partial n}{\partial t} + \nabla \cdot (-qn\mu_n \varepsilon \nabla \varphi + qD_n \nabla n) = qR \qquad \text{in } \Omega_{Si} \tag{1.43}$$
$$n = n_D \qquad \text{on } \Gamma_{D,Si} \tag{1.44}$$
$$\nabla n \cdot \mathbf{n} = 0 \qquad \text{on } \Gamma_{N,Si} \tag{1.45}$$
$$n(\mathbf{x}, t = 0) = p_0(\mathbf{x}) \qquad \mathbf{x} \in \Omega_{Si} \tag{1.46}$$

$$q\frac{\partial p}{\partial t} + \nabla \cdot (-qp\mu_p \varepsilon \nabla \varphi - qD_p \nabla p) = -qR \qquad \text{in } \Omega_{Si} \tag{1.47}$$
$$p = p_D \qquad \text{on } \Gamma_{D,Si} \tag{1.48}$$
$$\nabla p \cdot \mathbf{n} = 0 \qquad \text{on } \Gamma_{N,Si} \tag{1.49}$$
$$p(\mathbf{x}, t = 0) = p_0(\mathbf{x}) \qquad \mathbf{x} \in \Omega_{Si} \tag{1.50}$$

Relations (1.46) and (1.46) are the initial conditions, $n_0(\mathbf{x})$ and $p_0(\mathbf{x})$ being positive given data.

1.3 Physical Models for Semiconductors

As pointed out in Sect. 1.1, we need proper models for describing the mobility and the generation/recombination terms. In this section we provide a detailed analysis of these terms, also including a suitable modeling of the intrinsic concentration, bandgap and carrier driving force.

1.3.1 Carrier Mobility

The following *Einstein relation* estabilishes a link between carrier mobilities and their diffusivities

$$D_n = \frac{\mu_n k_b T}{q}\,, \qquad D_p = \frac{\mu_p k_b T}{q}\,. \tag{1.51}$$

Using (1.51) in equations (1.27) and (1.28) we can rewrite the current densities as:

$$\begin{aligned}\mathbf{J}_n &= qn\mu_n\mathbf{E} + q\frac{\mu_n k_b T}{q}\nabla n \\ &= -qn\mu_n\left(\nabla\varphi - \frac{\mu_n k_b T}{qn}\nabla n\right), \qquad (1.52)\\ \mathbf{J}_p &= qp\mu_p\mathbf{E} - q\frac{\mu_p k_b T}{q}\nabla p \\ &= -qp\mu_p\left(\nabla\varphi + \frac{\mu_p k_b T}{qp}\nabla p\right). \qquad (1.53)\end{aligned}$$

These two relations give rise to the mathematical definition of the quasi Fermi potentials φ_n and φ_p as:

$$\varphi_n := \varphi - V_{th}\ln\left(\frac{n}{n_i}\right) \qquad (1.54)$$

$$\varphi_p := \varphi + V_{th}\ln\left(\frac{p}{n_i}\right) \qquad (1.55)$$

so that the current densities can be expressed in the equivalent form:

$$\mathbf{J}_n = -qn\mu_n\nabla\varphi_n\,, \qquad \mathbf{J}_p = -qp\mu_p\nabla\varphi_p\,. \qquad (1.56)$$

These latter relationships highlight the fundamental role played by mobilities μ_n and μ_p in characterizing the conductive properties of a medium, thus great effort has to be made for their modeling.

Lattice Scattering

Semiconductor matierials can be described as perfect crystalline structures where the defects are completely ionized and occupy lattice positions. At temperatures different from the 0 K crystal lattice vibrates, generating *phonons*. These phonons are responsible for the scattering with the carriers travelling in the crystal. Increasing temperature will cause more scattering to occur, hence degradating mobility. In order to model the phonon scattering effect the following expression has been proposed [11]:

$$\mu_L = \mu_0\left(\frac{T}{T_0}\right)^{-\beta} \qquad (1.57)$$

where μ_0 is the reference mobility and β a properly fitted parameter at $T_0 = 300\,K$. Parameter values for electrons and holes, are reported in Tab. 1.1.

Parameter	Electrons	Holes	Unit of Measure
μ_0	1417.0	470.5	$\mathrm{cm^2V^{-1}s^{-1}}$
β	2.5	2.2	1

Table 1.1: Phonon scattering - parameter values at $T_0 = 300\,K$

Ionized Impurity Scattering
The presence of ions, used for obtain n/p-type region in an extrinsic semiconductor, is responsible for degradating the carrier mobilities: the charged nuclei break the regularity of the silicon lattice, introducing local perturbations to the electrostatic potential, thus interfering with the carrier trajectories.
A model for this phenomenon was proposed by Masetti et al. in [13] and can be expressed as follows:

$$\mu_{LI} = \mu_{min1} \exp\left(-\frac{P_c}{N_{tot}}\right) + \frac{\mu_L - \mu_{min2}}{1 + \left(\frac{N_{tot}}{C_r}\right)^{\alpha}} - \frac{\mu_1}{1 + \left(\frac{C_s}{N_{tot}}\right)^{\beta}} \tag{1.58}$$

where μ_L is the carrier mobility calculated by taking into account the sole lattice scattering (namely, using (1.57)), while N_{tot} is the sum of acceptor and donor densities, $N_{tot} = N_{tot}(\mathbf{x}) = N_D^+(\mathbf{x}) + N_A^-(\mathbf{x})$. Values for the other parameters are reported for silicon in Tab. 1.2.

Parameter	Electrons	Holes	Unit of Measure
μ_{min1}	52.2	44.9	$\mathrm{cm^2\,V^{-1}\,s^{-1}}$
μ_{min2}	52.2	0	$\mathrm{cm^2\,V^{-1}\,s^{-1}}$
μ_1	43.4	29.0	$\mathrm{cm^2\,V^{-1}\,s^{-1}}$
P_c	0	9.23×10^{16}	$\mathrm{cm^3}$
C_r	9.68×10^{16}	2.23×10^{17}	$\mathrm{cm^3}$
C_s	3.43×10^{20}	6.10×10^{20}	$\mathrm{cm^3}$
α	0.680	0.719	1
β	2.0	2.0	1

Table 1.2: Ionized impurities scattering - parameter values

High-Field Carrier Velocity Saturation
The presence of an electric field in a working semiconductor device, accelerates the mobile charges, thus their velocities increase, but speed values

cannot grow indefinitely. From a physical point of view, once the maximum value has been reached, the carrier extra energy is emitted under the form of optical phonons. To avoid unfeasible carrier velocities when $|\mathbf{E}| \to \infty$, an upper bound must be provided. Mathematically, we require that:

$$\lim_{|\mathbf{E}|\to\infty} \mu|\mathbf{E}| = v_{sat} < +\infty.$$

The Canali model [4] is a very common choice for implementing the aforementioned specification:

$$\mu = \frac{\mu_{low}}{\left[1 + \left(\frac{\mu_{low} F_{hfs}}{v_{sat}}\right)^{\beta}\right]^{1/\beta}} \tag{1.59}$$

where μ_{low} is the low-field mobility, F_{hfs} is the carrier driving force (that will be discussed in Sect. 1.3.4), while v_{sat} and β are given by

$$v_{sat} = v_0 \exp\left(\frac{300}{T}\right)^{v_{exp}}, \qquad \beta = \beta_0 \left(\frac{T}{300}\right)^{\beta_{exp}}. \tag{1.60}$$

All parameter values are reported in Tab. 1.3.

Parameter	Electrons	Holes	Unit of Measure
v_0	1.07×10^7	8.37×10^6	$\mathrm{cm\,s^{-1}}$
v_{exp}	0.87	0.52	1
β_0	1.109	1.213	1
β_{exp}	0.66	0.17	1

Table 1.3: Canali model - parameter values

Combining Mobility Models

To describe the carrier travelling as the result of different mechanisms, we need to assume appropriate combining rules. At low electric field the distinct contributions are assembled using the *Mathiessen rule*:

$$\mu = \left(\frac{1}{\mu_1} + \cdots + \frac{1}{\mu_N}\right)^{-1}. \tag{1.61}$$

The global mobility is thus computed as the harmonic average of the various mechanisms taking place during carrier motion. In conditions of high electric

field, once the low-field mobility has been determined using Mathiessen's rule, the resulting mobility is calculated by choosing a proper high-field model.
In conclusion, we can outline the process of characterizing carrier mobility as:

- compute the constant mobility (1.57);
- evaluate the Masetti model (1.58) and other possible scattering mechanisms using (1.61);
- apply the Canali model (1.59).

1.3.2 Generation-Recombination Phenomena

In thermodynamic equilibrium no net generation or recombination process can take place: in a typical semiconductor device under working conditions, this assumption obviously does not hold, then a non-zero generation (G) or recombination (R) rate must be calculated.
The general expression to evaluate the net R/G rate R is given by:

$$R(n,p) = (pn - n_i^2)F(n,p) \tag{1.62}$$

where the first term expresses the fact that, at equilibrium, the resulting rate must be null, while the scalar function $F(n,p)$ has to be provided according to the effect that has to be modeled. Finally, when different mechanisms are present, assembling many models is trivial: the separate contributions are just added together.

Shockley-Read-Hall Recombination
In indirect bandgap semiconductors, such as silicon, the most relevant phenomenon is the trap assisted generation-recombination, in which carriers can move from valence to conduction band and viceversa. Even if, in principle, carriers can jump up or down directly, the possibility of having enough energy is extremely small (band minima and maxima are misaligned). Trap states placed in the forbidden gap allow the particle momentum to change, hence making transitions possible. These spurious energy levels are generated by lattice imperfections -*deep defect levels*- that can significantly increase when dopants are inserted.
The global mechanism can be decomposed in the following two processes:

- an electron in the conduction band relaxes to the valence band via a trap state and there neutralizes a hole (R_{SRH});

- a hole in the valence band jumps into the conduction band via a trap state and there recombines with an electron (G_{SRH}).

The Shockley-Read-Hall formula provides the function F

$$F_{SRH}(n,p) = \frac{1}{\tau_n\,(n+\bar{n}) + \tau_p\,(p+\bar{p})} \tag{1.63}$$

with

$$\bar{n} = n_i \cosh\left(\frac{E_t - E_i}{k_B T}\right), \qquad \bar{p} = n_i \cosh\left(\frac{E_i - E_t}{k_B T}\right) \tag{1.64}$$

Parameters τ_n and τ_p are the carrier lifetimes [s^{-1}], while the value E_t represents the energy level [eV] of the trap state. The maximum recombination rate occurs when $E_t = E_i$ (i.e. when the trap is placed on the intrinsinc Fermi level) and typical values for carrier lifetimes lie in the range spanning from 1 µs to 1 ms, as reported in Tab. 1.4.

Parameter	Electrons	Holes	Unit of Measure
τ	1.0×10^{-5}	3.0×10^{-6}	s
E_t	0.0	0.0	eV

Table 1.4: Shockley-Read-Hall model - parameter values.

Auger Recombination

The Auger recombination is a three-particle process in which electron-hole pairs recombine in band-to-band transitions, giving the excess of energy to another electron or hole, that eventually will lose its energy by colliding with the lattice, hence relaxing to the bottom of the proper band.
Four different situations can occur:

- $R_{Au}^{2n,1p}$, where high-energy electron in the conduction band recombines with a hole in valence band, releasing the excess energy to another electron in the conduction band;

- $G_{Au}^{2n,1p}$, where an electron in the valence band jumps into the conduction band acquiring the required energy from a higher energy electron in the conduction band, consequently leaving a hole in the valence band;

- $R_{Au}^{2p,1n}$, is the same as the $R_{Au}^{2n,1p}$ recombination, but the roles of electrons and holes are exchanged;

- $G_{Au}^{2p,1n}$, is the same as the $G_{Au}^{2n,1p}$ generation, but the roles of electrons and holes are exchanged.

The whole process is quantitatively expressed by the function:

$$F_{Au}(n,p) = \Gamma_n n + \Gamma_p p \tag{1.65}$$

in which Γ_n and Γ_p take the name of Auger coefficients and represent the proper event probability. Their values are reported in Tab. 1.5.
Substituting the expression of F in (1.62) leads to the polynomial terms n^2p and p^2n, highlighting the three-particle interaction needed for the phenomenon to happen.

As a final note we point out that, being the Auger coefficients usually very small, the Auger effect becomes relevant only in case of very high dopant concentration.

Parameter	Electrons	Holes	Unit of Measure
Γ	2.9×10^{-31}	1.028×10^{-31}	$\mathrm{cm}^6\,\mathrm{s}^{-1}$

Table 1.5: Auger model - parameter values

Phonon-assisted Tunneling
Under certain circumstances -such as high potential drops across small intervals or narrow p-n junctions with high doping concentrations- the resulting energy bands exhibit a steep gradient. In these scenarios, the distance between bands gets considerably reduced and the small spatial gap allows the wavefunctions of electrons in valence and conduction to overlap, hence making a transition possible. Even though no extra energy is required to perform the transition, a change in the particle momentum is required; this occurs via a phonon collision, as shown in Fig. 1.2.

In his work, Schenk [17] rigorously derives an expression for the phonon-assisted tunneling and obtains a result that, coherently with equation (1.62), reads as:

$$\begin{aligned} R(n,p) = & \frac{AF^{\frac{7}{2}}}{(n+n_i)(p+n_i)} \\ & \times \left[\frac{(F_{cr}^{\mp})^{-\frac{3}{2}} \exp\left(-\frac{F_{cr}^{\mp}}{F}\right)}{\exp\left(-\frac{\hbar\omega_{ph}}{k_B T}\right) - 1} + \frac{(F_{cr}^{\pm})^{-\frac{3}{2}} \exp\left(-\frac{F_{cr}^{\pm}}{F}\right)}{1 - \exp\left(-\frac{\hbar\omega_{ph}}{k_B T}\right)} \right] \end{aligned} \tag{1.66}$$

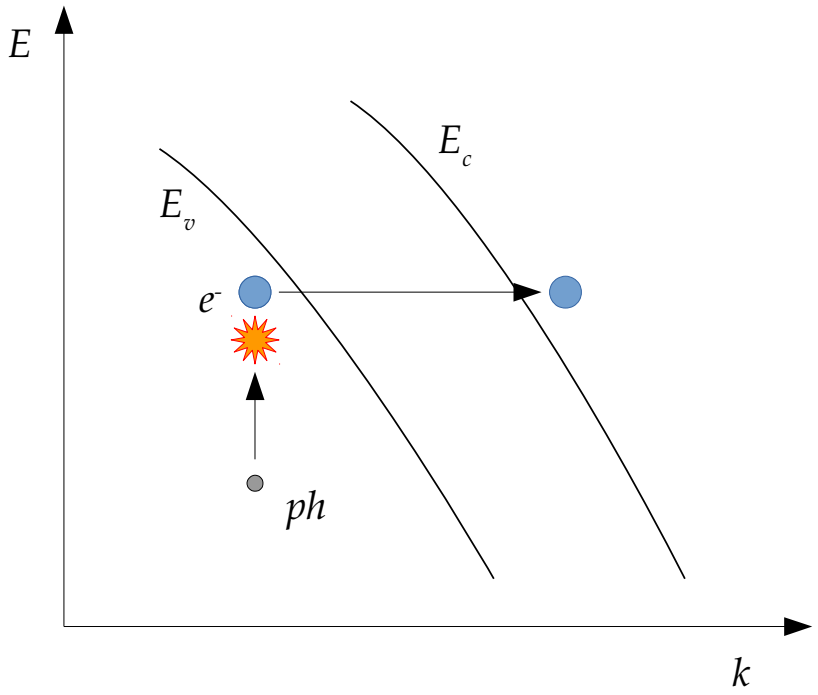

Figure 1.2: Representation of the phonon-assisted tunneling effect in the E-k plane: colliding with the phonon (ph), the electron (e^-) is able to move from the valence to the conduction band crossing the forbidden gap.

where we have denoted by F the electric field magnitude, while $F_{cr}^{\pm}$ is the critical field strength and is given by

$$F_{cr}^{\pm} = B\left(E_{gap} \pm \hbar\omega_{ph}\right) , \tag{1.67}$$

the quantity $\hbar\omega_{ph}$ being the acoustic phonon energy. The other parameters are summarized in Tab. 1.6. The upper sign in (1.66) and (1.67) refers to tunneling generation ($np < n_i^2$), while the lower one applies in the case of recombination ($np > n_i^2$).

Parameter	Value	Unit of Measure
A	8.977×10^{20}	s
B	2.14667×10^{7}	eV
$\hbar\omega_{ph}$	18.6	meV

Table 1.6: Schenk model - parameter values.

Impact ionization
If the electric field magnitude is high, carriers can acquire enough kinetic energy to generate an electron-hole pair by breaking a lattice bond when a collision occurs. The three particles can in turn generate additional pairs by impacting other atoms and ionizing them as well, causing an avalanche generation effect.
Models describing impact ionization phenomena assume a slighlty different form than (1.62). The generic expression relies on Chynoweth's law [5]:

$$F_{II} = \alpha_n n|\mathbf{v_n}| + \alpha_p p|\mathbf{v_n}| \ . \tag{1.68}$$

Coefficients α_n and α_p can be interpreted as the probability for unit length for an electron or hole to collide with an atom and to ionize it. Among the various possibilities, we choose the Van Overstraeten-De Man model [19], which gives:

$$\alpha_\nu(F_{ava}) = \gamma a_\nu \exp\left(-\frac{\gamma b_\nu}{F_{ava}}\right) \qquad \nu = n, p \tag{1.69}$$

with

$$\gamma = \frac{\tanh\left(\dfrac{\hbar\omega_{op}}{2k_B T_0}\right)}{\tanh\left(\dfrac{\hbar\omega_{op}}{2k_B T}\right)} . \tag{1.70}$$

The quantity $\hbar\omega_{op}$ is the optical phonon energy, while the scalar value F_{ava} is the avalanche field, that can be set as either equal to the quasi Fermi potential gradient or the electric field component parallel to the current density (see Sect. 1.3.4). Parameter values are reported in Tab. 1.7 (notice the dependency on the electric field magnitude).

Parameter	Electrons	Holes	Valid Range	Unit of Measure
E_0	4.0×10^5	4.0×10^5		Vcm^{-1}
a_{high}	7.03×10^5	6.71×10^5	$E_0 \div 6.0 \times 10^5$	cm^{-1}
a_{low}	7.03×10^5	1.582×10^6	$1.75 \times 10^5 \div E_0$	cm^{-1}
b_{high}	1.231×10^6	1.693×10^6	$E_0 \div 6.0 \times 10^5$	Vcm^{-1}
b_{low}	1.231×10^6	2.036×10^6	$1.75 \times 10^5 \div E_0$	Vcm^{-1}
$\hbar\omega_{op}$	0.063	0.063		eV

Table 1.7: Van Overstraeten-De Man model - parameter values

1.3.3 Bandgap Narrowing and Intrinsic Concentration

As many other quantities, such as the mobility values previously treated, the energy bandgap is affected by temperature. Even though the nature of this phenomenon still presents unclarified points (especially at low temperature), it is believed that this dependence arises from two different effects:

- a shift in the relative position of conduction and valence bands due to lattice dilatation/compression;
- a change induced by electron-phonon interaction;

It can be shown that the bandgap is related with temperature through:

$$\Delta E_{gap} \propto T^2 \qquad \text{for } T \ll \Theta \tag{1.71}$$

$$\Delta E_{gap} \propto T \qquad \text{for } T \gg \Theta \tag{1.72}$$

Θ being the material *Debye temperature*. According to (1.71) and (1.72), Varshni [20], proposed the following expression:

$$E_{gap}(T) = E_{gap}(0) - \frac{\alpha T^2}{T + \beta} \tag{1.73}$$

where $E_{gap}(0)$ is the bandgap energy at 0 K, and α and β are properly fitted parameters (values for silicon are reported in Tab. 1.8).

Parameter	Value	Unit of Measure
$E_{gap}(0)$	1.1696	eV
α	4.74×10^{-4}	eVK^{-1}
β	636	K

Table 1.8: Thermal bandgap model - parameter values.

Intrinsic concentration also depends on temperature and not only through the energy gap, but also by means of the effective density of states N_C and N_V

$$n_i = \sqrt{N_C(T) N_V(T)} \exp\left(-\frac{E_{gap}}{2k_b T}\right). \tag{1.74}$$

A possibility for expliciting the temperature dependence is represented by the following expressions:

$$N_C(T) = 2\left(\frac{2\pi m_e^* k_b T}{h^2}\right)^{\frac{3}{2}} = N_C(300K)\left(\frac{T}{300K}\right)^{\frac{3}{2}}, \tag{1.75}$$

$$N_V(T) = 2\left(\frac{2\pi m_h^* k_b T}{h^2}\right)^{\frac{3}{2}} = N_V(300K)\left(\frac{T}{300K}\right)^{\frac{3}{2}}. \tag{1.76}$$

A second approach is to consider the expression of the effective mass. For electrons we have:

$$m_e^* = 6^{\frac{2}{3}} \left(m_l m_t^2\right)^{\frac{2}{3}} , \tag{1.77}$$

$$\frac{m_t}{m_0} = a\frac{E_{gap}(0)}{E_{gap}(T)} \tag{1.78}$$

and N_C becomes

$$N_C(T) = N_{C,0}\left(\frac{m_e^*(T)}{m_0}\right)^{\frac{2}{3}}\left(\frac{T}{300K}\right)^{\frac{2}{3}} . \tag{1.79}$$

For the holes, the effective mass expression is:

$$\frac{m_h^*}{m_0} = \frac{a + bT + cT^2 + dT^3 + eT^4}{1 + fT + gT^2 + hT^3 + iT^4} \tag{1.80}$$

and the resulting density of states is

$$N_V(T) = N_{V,0}\left(\frac{m_h^*(T)}{m_0}\right)^{\frac{2}{3}}\left(\frac{T}{300K}\right)^{\frac{2}{3}} . \tag{1.81}$$

Parameter values are shown in Tab. 1.9 for electrons and Tab. 1.10 for holes.

Parameter	Value	Unit of Measure
m_0	9.109×10^{-31}	kg
m_l	$0.9163m_0$	kg
a	0.1905	1
$N_{C,0}$	2.5094×10^{19}	cm^{-3}
$N_C(300K)$	2.89×10^{19}	cm^{-3}

Table 1.9: Electron effective mass and density of states in conduction band - parameter values.

1.3.4 Driving Force

In some of the previous models, the driving force has been mentioned but not specified. Two are the main approaches for evaluating it:

- the gradient of quasi-Fermi potential

$$F_{d,\nu} = |\nabla\varphi_\nu| \qquad \nu = n, p \tag{1.82}$$

Parameter	Value	Unit of Measure
m_0	9.109×10^{-31}	kg
a	0.4435870	1
b	0.3609528×10^{-2}	K^{-1}
c	0.1173515×10^{-3}	K^{-2}
d	0.1263218×10^{-5}	K^{-3}
e	0.3025581×10^{-8}	K^{-4}
f	0.4683382×10^{-2}	K^{-1}
g	0.2286895×10^{-3}	K^{-2}
h	0.7469271×10^{-6}	K^{-3}
i	0.1727481×10^{-8}	K^{-4}
$N_{V,0}$	2.5094×10^{19}	cm^{-3}
$N_V(300K)$	3.14×10^{19}	cm^{-3}

Table 1.10: Hole effective mass and density of states in conduction band - parameter values.

- the electric field component parallel to the current density

$$F_{d,\nu} = \frac{\mathbf{E} \cdot \mathbf{J}_\nu}{|\mathbf{J}_\nu|} \qquad \nu = n, p \tag{1.83}$$

where $F_{d,\nu}$ indicates the carrier driving force. The choice of the approach significantly affects the performance of a numerical simulation. A comparison between (1.82) and (1.83) will be carried out in Chapt. 3.

Chapter 2

Numerical Discretization and Solution Algorithms

The Drift-Diffusion model is a highly nonlinear system of PDEs. An analytical solution is possible only under strong simplifications and/or in specific working conditions, so that an accurate numerical approach is required to treat the simulation of a realistic device. In this chapter we describe the methodologies adopted for solving the stationary version of equations (1.40)-(1.50) and, then, we analyze the techniques required in the time dependent case.

2.1 Gummel Map

Originally proposed in [7], the Gummel map algorithm is an iterative method used to solve (1.40)-(1.50) in stationary conditions. The solving procedure is outlined in Algorithm 1.

For reading benefits, we now proceed with a detailed description of the method: the nonlinearity is limited to the sole Poisson equation (1.40), whereas the continuity equations are solved in a linearized form. Let us start with (1.40): we replace the electron and hole concentrations with the Maxwell-Boltzmann statistics (1.35)-(1.36), obtaining

$$\nabla \cdot (-\varepsilon \nabla \varphi) - q n_i \left(\exp\left(\frac{\varphi_p - \varphi}{V_{th}} \right) - \exp\left(\frac{\varphi - \varphi_n}{V_{th}} \right) \right) - qD = 0 \,. \quad (2.1)$$

Because of its nonlinearity, in order to solve equation (2.1) we use the Newton method, that can be formulated in a generalized abstract form as:

Algorithm 1: Gummel Map

Input:
φ^0, electrostatic potential initial guess;
n^0, electron density initial guess;
p^0, hole density initial guess;
tol_{NLP}, Nonlinear Poisson tolerance;
tol_{GM}, Gummel Map tolerance;

$i = 0$
$tol = \infty$
while $tol \geq tol_{GM}$ **do**
  $i = i + 1$
  φ_n^{i-1}, $\varphi_p^{i-1} \leftarrow$ compute quasi-Fermi potential(n^{i-1}, p^{i-1})
  $k = 0$
  while $tol \geq tol_{NLP}$ **do**
    $\delta\varphi^k \leftarrow$ Solve NLP$(\varphi^{k-1}, \varphi_n^{i-1}, \varphi_p^{i-1})$
    $\varphi^{k+1} = \varphi^k + \delta\varphi^k$
    $tol \leftarrow$ compute NLP tolerance (φ^{k+1})
    $k = k + 1$
  end
  $\varphi^i = \varphi^k$
  $n^i \leftarrow$ solve LEC$(\varphi^i, n^{i-1}, p^{i-1})$
  $p^i \leftarrow$ solve LHC$(\varphi^i, n^{i-1}, p^{i-1})$
  $tol \leftarrow$ compute GM tolerance$(n^i, p^i, n^{i-1}, p^{i-1})$
end

Newton Method

Let $(X, \|\cdot\|_X), (Y, \|\cdot\|_Y)$ be two Banach spaces and $F : X \mapsto Y$ a Frechét differentiable function operator. Given an initial datum $U_0 \in X$ and a positive tolerance $tol > 0$, for all $k \geq 0$ solve the following linear problem:

$$\begin{cases} F'(U^k; \delta U^k) = -F(U^k) \\ U^{k+1} = U^k + \delta U^k \end{cases} \tag{2.2}$$

until

$$\|F(U^{k+1})\|_Y < tol \tag{2.3}$$

In our case the operator F is given by the left-hand side of (2.1), hence calculating the Frechét derivative we have

$$F'(\varphi; \delta\varphi) = -\nabla\cdot(\varepsilon\nabla\delta\varphi) + \frac{qn_i}{V_{th}} \left(\exp\left(\frac{\varphi_p - \varphi}{V_{th}}\right) + \exp\left(\frac{\varphi - \varphi_n}{V_{th}}\right)\right) \delta\varphi \tag{2.4}$$

and the Newton method reads:

$$\begin{cases} \nabla \cdot (-\varepsilon\nabla\delta\varphi^k) + \sigma^k\delta\varphi^k = f^k & \text{in } \Omega \\ \delta\varphi^k = 0 & \text{on } \Gamma_D \\ \nabla\delta\varphi^k \cdot \mathbf{n} = 0 & \text{on } \Gamma_N \\ \varphi^{k+1} = \varphi^k + \delta\varphi^k \end{cases} \tag{2.5}$$

where

$$\sigma^k = \begin{cases} \dfrac{qn_i}{V_{th}} \left(\exp\left(\dfrac{\varphi_p - \varphi^k}{V_{th}}\right) + \exp\left(\dfrac{\varphi^k - \varphi_n}{V_{th}}\right)\right) & \text{in } \Omega_{Si} \\ 0 & \text{in } \Omega_{ox} \end{cases} \tag{2.6}$$

and

$$f^k = \begin{cases} \nabla \cdot (-\varepsilon\nabla\varphi^k) - qn_i \left(\exp\left(\frac{\varphi_p - \varphi^k}{V_{th}}\right) - \exp\left(\frac{\varphi^k - \varphi_n}{V_{th}}\right)\right) - qD & \text{in } \Omega_{Si} \\ \nabla \cdot (-\varepsilon\nabla\varphi^k) & \text{in } \Omega_{ox} \end{cases} \tag{2.7}$$

After the Nonlinear Poisson (NLP) equation (2.1) has been solved, the electrostatic potential is updated within the Gummel map

$$\varphi^i = \varphi^{\bar{k}}$$

where i indicates the Gummel map iteration, while $\bar{k}$ is the index of Newton's algorithm at which the convergence criterion is satisfied. This potential is

then fed into the linearized continuity equations using the technique known as the *lagging approach* [10]. The main idea is to compute the R/G rate $R(n,p)$, written in the generic form (1.62), using the solution from the previous iteration. Therefore for a certain iteration i we set:

$$\begin{aligned} R_n^i &= (n^i p^{i-1} - n_i^2) F(n^{i-i}, p^{i-1}) \qquad \text{for electrons,} \\ R_p^i &= (n^{i-1} p^i - n_i^2) F(n^{i-i}, p^{i-1}) \qquad \text{for holes.} \end{aligned}$$

Exploiting these expressions, we can write the problems for the steady-state linearized electron and hole continuity equations (denoted by LEC and LHC, respectively). Equation (1.43) becomes

$$\text{(LEC)} \qquad \begin{aligned} \nabla \cdot (q n^i \mu_n \varepsilon \nabla \varphi^i - q D_n \nabla n^i) &= -q R_n^i && \text{in } \Omega_{Si} \\ n^i &= n_D && \text{on } \Gamma_{D,Si} \\ \nabla n^i \cdot \mathbf{n} &= 0 && \text{on } \Gamma_{N,Si} \end{aligned} \tag{2.8}$$

while (1.47) is given by

$$\text{(LHC)} \qquad \begin{aligned} \nabla \cdot (-q p^i \mu_p \varepsilon \nabla \varphi^i - q D_p \nabla p^i) &= -q R_p^i && \text{in } \Omega_{Si} \\ p^i &= p_D && \text{on } \Gamma_{D,Si} \\ \nabla p^i \cdot \mathbf{n} &= 0 && \text{on } \Gamma_{N,Si} \end{aligned} \tag{2.9}$$

It is useful to split the R/G term in (2.8) and (2.9) isolating the production and reaction contributions:

$$\nabla \cdot (+q n^i \mu_n \varepsilon \nabla \varphi^i - q D_n \nabla n^i) + q \sigma_n^{i-1} n^i = q f_n^{i-1} \tag{2.10}$$

$$\nabla \cdot (-q p^i \mu_p \varepsilon \nabla \varphi^i - q D_p \nabla p^i) + q \sigma_p^{i-1} p^i = q f_p^{i-1} \tag{2.11}$$

having set

$$\begin{aligned} \sigma_n^{i-1} &= p^{i-1} F(n^{i-i}, p^{i-1}) & \qquad \sigma_p^{i-1} &= n^{i-1} F(n^{i-i}, p^{i-1}) \\ f_n^{i-1} &= n_i^2 F(n^{i-i}, p^{i-1}) & \qquad f_p^{i-1} &= n_i^2 F(n^{i-i}, p^{i-1}) \end{aligned}$$

Problems (2.8) and (2.9) are solved sequentially providing the carrier densities n and p which are then used to recompute the quasi-Fermi potentials φ_n and φ_p, needed by the Poisson equation, using (1.54) and (1.55). Then, the Gummel map iteration counter is increased and the procedure continues until convergence.
It is interesting to notice that the algebraic counterpart of the above treatment of the R/G term corresponds to the Jacobi iterative method for linear systems. Another possibility would have been to use the latest computed

electron density (n^i) in (2.11), instead of the previous one (n^{i-1}), leading to a Gauss-Seidel iterative approach.

The criteria that are used to monitor the convergence of the Gummel map are based on the residual of the Nonlinear Poisson solver and the difference between solutions of two successive iterates of the map, both evaluated using suitable norms, as:

$$\begin{aligned} \|F(\varphi^k)\|_{L^2} &< tol_{NLP}\,, \\ \|\varphi^i - \varphi^{i-1}\|_{L^\infty} + \|n^i - n^{i-1}\|_{L^\infty} + \|p^i - p^{i-1}\|_{L^\infty} &< tol_{GM}\,. \end{aligned}$$

where tol_{NLP} and tol_{GM} are positive predefined tolerances. With the above choice, it has been proved in [10] that the Gummel map algorithm converges to the exact solution of the Drif-Diffusion with a linear rate. Regardless such theoretical results, in practice the method often exhibits a higher convergence rate (superlinear).

The Gummel map is not the only viable choice for solving the stationary Drift-Diffusion system, another common approach is the so called fully coupled Newton algorithm. Albeit the latter one attains a convergence rate substantially higher (quadratic),the former one still has a few non negligible advantages:

- lesser computational requirements, because at each iteration 3 linear systems of dimension N_{dof}^2 have to be solved instead of a system of dimension $(3N_{dof})^2$;
- more insensitivity to the initial guess, which is an extremely valuable feature especially in a 3D context, where the problem of finding a good initial guess is often non trivial.

2.2 Weak Formulation

In order to numerically solve the above Gummel map, a finite element scheme is adopted in our work. Let us now consider the treatment of each of the three involved equations.

2.2.1 Nonlinear Poisson Equation

To discretize the NLP equation, that is a Diffusion-Reaction (DR) problem, we need to introduce the Sobolev space $H^1(\Omega)$

$$H^1(\Omega) = \{v \in L^2(\Omega) : \|\nabla v\|_{L^2(\Omega} < \infty\}$$

and the associated subspace $H^1_{\Gamma_D}(\Omega)$ composed by functions vanishing on the boundary $\Gamma_D \subseteq \partial\Omega$:

$$H^1_{\Gamma_D}(\Omega) = \{v \in H^1(\Omega) : v|_{\Gamma_D} = 0\}\,.$$

Multiplying equation (2.5) by a test function $v \in V = H^1_{\Gamma_D}(\Omega)$ and integrating on the whole domain we obtain:

$$\int_\Omega \nabla \cdot (-\varepsilon \nabla \delta\varphi^k) v \, d\Omega + \int_\Omega \sigma^k \delta\varphi^k v \, d\Omega = \int_\Omega f^k v \, d\Omega\,.$$

Applying Green's theorem to the first term, we have:

$$\begin{aligned}\int_\Omega \nabla \cdot (-\varepsilon \nabla \delta\varphi^k) v \, d\Omega &= \int_\Omega \varepsilon \nabla \delta\varphi^k \nabla v \, d\Omega - \int_{\partial\Omega} \varepsilon \nabla \delta\varphi^k \cdot \mathbf{n} v \, d\Gamma \\ &= \int_\Omega \varepsilon \nabla \delta\varphi^k \nabla v \, d\Omega - \int_{\Gamma_D} \varepsilon \nabla \delta\varphi^k \cdot \mathbf{n} v \, d\Gamma - \int_{\Gamma_N} \varepsilon \nabla \delta\varphi^k \cdot \mathbf{n} v \, d\Gamma \\ &= \int_\Omega \varepsilon \nabla \delta\varphi^k \nabla v \, d\Omega\end{aligned}$$

beacuse functions in $H^1_{\Gamma_D}(\Omega)$ have null trace on Γ_D and the homogeneous boundary condition. We can therefore state the weak formulation for the generic Newton iteration of the nonlinear Poisson equation as follows:

Linearized NLP - Weak Formulation

Find $\delta\varphi^k \in V$ s.t.:

$$a^k(\delta\varphi^k, v) = L^k(v) \qquad \forall v \in V \tag{2.12}$$

where $a^k : V \times V \mapsto \mathbb{R}$ and $L^k : V \mapsto \mathbb{R}$ are defined as

$$\begin{aligned}a^k(u, v) &= \int_\Omega \varepsilon \nabla u \nabla v \, d\Omega + \int_\Omega \sigma^k u v \, d\Omega\,, \\ L^k(v) &= \int_\Omega f^k v \, d\Omega\,.\end{aligned}$$

The analysis of well-posedness can be carried out using Lax-Milgram theorem. Physically consistent assumptions on the involved quantities imply that:

- $0 < \varepsilon_m \leq \varepsilon(x) \leq \varepsilon_M$ a.e. in Ω;
- $\sigma^k \in L^\infty(\Omega)$ and $\sigma^k > 0$ a.e. in $\Omega \;\; \forall k > 0$;
- $f^k \in L^2(\Omega) \;\; \forall k > 0$.

Using these relationships it is possibile to prove the following properties:

- Continuity of $a^k(\,\cdot\,,\,\cdot\,)$

$$|a^k(u,v)| \leq \left(\varepsilon_M + c_P^2 \|\sigma^k\|_{L^\infty(\Omega)}\right) \|u\|_V \|v\|_V \qquad \forall\, u, v \in V$$

- Coercivity of $a^k(\,\cdot\,,\,\cdot\,)$

$$a^k(u,u) \geq \varepsilon_m \|u\|_V^2 \qquad \forall\, u \in V$$

- Continuity of L^k

$$|L^k(v)| \leq c_P \|f\|_{L_2(\Omega)} \|v\|_V \qquad \forall\, v \in V$$

where c_P is the Poincaré constant associated with the domain Ω and the norm $\|\cdot\|_V$ is defined as:

$$\|\phi\|_V = \|\nabla\phi\|_L^2(\Omega) \qquad \forall\, \phi \in V\,. \tag{2.13}$$

2.2.2 Continuity Equations

In the following we consider the sole electron continuity equation, being the one related to holes treated similarly. Equation (2.10) can be rewritten as a diffusion-advection-reaction (DAR) problem in conservative form:

$$\begin{cases} \nabla\cdot(-D_n\nabla n) + \nabla\cdot(\boldsymbol{\beta}_n^i n) + \sigma_n^{i-1} n = f_n^{i-1} & \text{in } \Omega_{Si} \\ n^i = n_D & \text{on } \Gamma_{D,Si} \\ \nabla n^i \cdot \mathbf{n} = 0 & \text{on } \Gamma_{N,Si} \end{cases} \tag{2.14}$$

where the transport term coefficient $\boldsymbol{\beta}_n^i$ is defined as:

$$\boldsymbol{\beta}_n^i = \mu_n \nabla\varphi^i\,.$$

We multiply the first equation in (2.14) by a test function $v \in V = H^1_{\Gamma_{D,Si}}(\Omega_{Si})$ (note that both the domain and the Dirichlet boundary have been changed according to the considerations made in Sect. 1.2) and integrate over the domain Ω_{Si}. This leads to the following weak formulation for the linearized electron continuity problem:

LEC - Weak Formulation

Find $n^i \in V = H^1_{\Gamma_{D,Si}}(\Omega_{Si})$ s.t.:

$$a_i(n^i, v) = L_i(v) \qquad \forall v \in V \tag{2.15}$$

where $a^i : V \times V \mapsto \mathbb{R}$ and $L^i : V \mapsto \mathbb{R}$ are defined as

$$a^i(u,v) = \int_{\Omega_{Si}} D_n \nabla u \nabla v \, d\Omega - \int_{\Omega_{Si}} \boldsymbol{\beta}^i_n u \cdot \nabla v \, d\Omega + \int_{\Omega_{Si}} \sigma^i_n uv \, d\Omega \,,$$
$$L^i(v) = \int_{\Omega_{Si}} f^i_n v \, d\Omega \,.$$

To carry out the anaysis of well-posedness it is useful to introduce the Slotboom variable u_n:

$$u_n := n_i \exp\left(-\frac{\varphi_n}{V_{th}}\right) \tag{2.16}$$

which implies

$$n = n_i \exp\left(\frac{\varphi}{V_{th}}\right) u_n \,.$$

Notice that

$$\nabla u_n = \exp\left(-\frac{\varphi}{V_{th}}\right) \nabla n - \exp\left(-\frac{\varphi}{V_{th}}\right) \frac{n}{V_{th}} \nabla \varphi$$

and hence, using Einstein relation (1.51), we get

$$\nabla \cdot \left(-D_n \exp\left(\frac{\varphi}{V_{th}}\right) \nabla u_n\right) = \nabla \cdot \left(-D_n \nabla n + \mu_n n \nabla \varphi\right) \,.$$

We can then write (2.14) in self-adjoint form as

$$\begin{cases} \nabla \cdot \left(-D_n \exp\left(\frac{\varphi}{V_{th}}\right) \nabla u_n\right) + \sigma^{i-1}_n \exp\left(\frac{\varphi}{V_{th}}\right) u_n = f^{i-1}_n & \text{in } \Omega_{Si} \\ u_n = n_D \exp\left(-\frac{\varphi}{V_{th}}\right) & \text{on } \Gamma_{D,Si} \\ \nabla u_n \cdot \mathbf{n} = 0 & \text{on } \Gamma_{N,Si} \end{cases} \tag{2.17}$$

Proceeding as before, the weak formulation associated with (2.17) reads as

Slotboom-LEC - Weak Formulation

Find $u_n^i \in V = H^1_{\Gamma_{D,Si}}(\Omega_{Si})$ s.t.:

$$\tilde{a}_i(u_n^i, v) = \widetilde{L}_i(v) \qquad \forall v \in V \tag{2.18}$$

where $\tilde{a}^i : V \times V \mapsto \mathbb{R}$ and $\widetilde{L}^i : V \mapsto \mathbb{R}$ are defined as

$$\tilde{a}^i(u,v) = \int_{\Omega_{Si}} D_n \exp\left(\frac{\varphi}{V_{th}}\right) \nabla u \nabla v \, d\Omega + \int_{\Omega_{Si}} \sigma_n^i \exp\left(\frac{\varphi}{V_{th}}\right) uv \, d\Omega \,,$$

$$\widetilde{L}^i(v) = \int_{\Omega_{Si}} f_n^i v \, d\Omega \; = L^i(v).$$

We will furthermore require that $\forall i > 0$:

- $0 < d_m \leq D_n \exp\left(\frac{\varphi}{V_{th}}\right) \leq d_M$ a.e. in Ω_{Si} ;
- $\sigma_n^i \exp\left(\frac{\varphi}{V_{th}}\right) \in L^\infty(\Omega_{Si})$ and $\sigma_n^i \geq 0$ a.e. in Ω_{Si};
- $f_n^i \in L^2(\Omega_{Si})$.

Using the same arguments applied in the NLP case, it is possible to prove that the hypothesis of the Lax-Milgram theorem are verified:

- Continuity of $\tilde{a}^i(\,\cdot\,,\,\cdot\,)$

$$|\tilde{a}^i(u,v)| \leq \left(d_M + c_P^2 \|\sigma_n^i \exp\left(\frac{\varphi}{V_{th}}\right)\|_{L^\infty(\Omega_{Si})}\right) \|u\|_V \|v\|_V \qquad \forall\, u, v \in V$$

- Coercivity of $\tilde{a}^i(\,\cdot\,,\,\cdot\,)$

$$\tilde{a}^i(u,u) \geq d_m \|u\|_V^2 \qquad \forall\, u \in V$$

- Continuity of $\widetilde{L}^i$

$$|\widetilde{L}^i(v)| \leq c_P \|f\|_{L_2(\Omega)} \|v\|_V \qquad \forall\, v \in V$$

Having proved that (2.18) is uniquely solvable, the existence and uniqueness of the solution n^i of (2.15) immediately follows from relation (2.16).

2.3 Finite Element Approximation

Let $\{\mathcal{T}_h\}_{h>0}$ be a family of simplicial partitions of Ω such that $\cup_{K\in\mathcal{T}_h} K = \overline{\Omega}_h \sim \overline{\Omega}$ where, for simplicity, we assume that the approximating domain, Ω_h, coincides exactly with the original one, Ω (i.e., Ω is a polyhedron). The positive parameter h represents the maximum simplex diameter:

$$h := \max_{K\in\mathcal{T}_h} h_K, \qquad h_K = \max_{\mathbf{x},\mathbf{y}\in K} |\mathbf{x}-\mathbf{y}| \,.$$

Furthermore we assume that the following *regularity condition* holds for each grid $\mathcal{T}_h$: there exists a positive constant δ such that

$$\frac{h_K}{\rho_K} \leq \delta \quad \forall K \in \mathcal{T}_h \tag{2.19}$$

where ρ_K is the *sphericity* of K (namely, the diameter of the inscribed hypersphere). Given a suitable Sobolev space V, a generic elliptic problem can be weakly formulated as:

$$\text{find } u \in V \text{ such that: } a(u,v) = F(v) \quad \forall v \in V \tag{2.20}$$

Introducing the family of approximating finite-dimensional spaces $\{V_h\}_{h>0}$ satisfying

$$V_h \subset V, \quad \dim(V_h) = N_h < \infty \quad \forall h > 0$$

we are able to state the *Galerkin formulation* of problem (2.20), which reads:

$$\text{find } u_h \in V_h \text{ such that: } a(u_h,v_h) = F(v_h) \quad \forall v_h \in V_h. \tag{2.21}$$

From different choices for the discrete space V_h, different numerical schemes arise. In this thesis we consider the choice leading to the finite element approximation of (2.20).

2.3.1 Nonlinear Poisson Equation

In order to numerically solve the generic Newton iteration of the Nonlinear Poisson problem (2.12), we discretize the Sobolev space $V = H^1_{\Gamma_D}(\Omega)$ with linear finite elements, namely the space of continuous piecewise linear functions over $\mathcal{T}_h$:

$$V_h = X^1_h(\Omega) = \{v_h \in C^0(\Omega) : v_h|_K \in \mathbb{P}_1(K), \forall K \in \mathcal{T}_h\} \,. \tag{2.22}$$

We can hence state the finite element formulation of problem (2.12) as follows:

Linearized NLP - FE Formulation

Find $\delta\varphi_h^k \in V_h \cap H^1_{\Gamma_D}(\Omega)$ s.t.:

$$a^k(\delta\varphi_h^k, v_h) = L^k(v_h) \qquad \forall v_h \in V_h \tag{2.23}$$

Exploiting the usual Lagrangian basis composed by hat (or tent) functions $\{\psi\}_{j=1}^{N_h}$, where $N_h = \dim(X_h^1(\Omega)$, we can write each element of $X_h^1(\Omega)$ in the following way:

$$v_h(x) = \sum_{j=1}^{N_h} v_j \psi_j(x)\,. \tag{2.24}$$

Therefore, equation (2.23) becomes:

$$\sum_{j=1}^{N_h} \delta\varphi_j^k a^k(\psi_j, \psi_i) = L^k(\psi_i) \qquad \forall i \in \{1, \dots, N_h\}.$$

This leads to the algebraic counterpart of problem (2.23), which reads as:

Linearized NLP - Algebraic Formulation

Find $\delta\boldsymbol{\varphi}^k \in \mathbb{R}^{N_h}$ s.t.:

$$\mathbf{A}^k \delta\boldsymbol{\varphi}^k = \mathbf{b}^k \tag{2.25}$$

where $\mathbf{A}^k \in \mathbb{R}^{N_h \times N_h}$ and $\mathbf{b}^k \in \mathbb{R}^{N_h}$ are defined as

$$[\mathbf{A}^k]_{i,j} = a^k(\psi_j, \psi_i)\,,$$
$$[\mathbf{b}^k]_i = L^k(\psi_i)\,.$$

Expanding the expression for the matrix coefficients

$$[\mathbf{A}^k]_{i,j} = [\mathbf{S}^k]_{i,j} + [\mathbf{N}^k]_{i,j} = \int_\Omega \varepsilon \nabla\psi_i \nabla\psi_j \, d\Omega + \int_\Omega \sigma^k \psi_i \psi_j \, d\Omega$$

we can recognize the two separate contributions of the *stiffness matrix* $\mathbf{S}^k$ and the *mass matrix* $\mathbf{N}^k$ to the global matrix. To attain better numerical properties the latter one is evaluated using the *trapezoidal rule*, which results in the *lumping* of matrix $\mathbf{N}^k$. This approach is motivated by the fact that with linear finite elements we expect a linear convergence rate ([15], Thm. 3.6), therefore such quadrature formula is accurate enough for our purposes.

Note that Dirichlet conditions are not explicitly present in (2.25), therefore they should be incorporated into the system matrix itself. A way to achieve that is the *diagonalization* technique, in which the rows corresponding

to Dirichlet boundary nodes are set identically to zero except for the diagonal entry. Setting the right-hand side at the corresponding index equal to the the associated boundary value will ensure Dirichlet condition to be satisfied exactly. Namely, $\forall i' \in \{i \in \{1, \ldots, N_h\} : i \text{ is a Dirichlet boundary node}\}$:

$$[\mathbf{A}^k]_{i',j} = \begin{cases} 0 \text{ if } j \neq i' \\ \gamma \text{ if } j = i' \end{cases} \quad , \qquad [\mathbf{b}^k]_{i'} = \gamma \varphi_D(\mathbf{x}_{i'}) \, . \tag{2.26}$$

To ensure a good balancing of the stiffness matrix accounting for Dirichlet boundary conditions the coefficient $\gamma \neq 0$ has been set equal to the orginal diagonal entry.

Finally, to avoid overshoot issues arising from the Newton update step (2.1), a damping procedure based on the Deuflhard criterion [6] is performed as described in [3].

2.3.2 Continuity equations

It is a well-known fact that diffusion-advection problems are very often difficult to treat with the standard finite element discretization emanating from the weak formulation (see [15], Chapter 5). In such a case, when the drift component is dominant the computed solution may exhibit undesired spurious oscillations. Reducing the grid step size will eventually eliminate this numerical instability, but the computational effort required could be unaffordable. To overcome this problem, several approaches have been proposed in the literature: the one we have adopted is the edge-averaged finite element (EAFE) scheme. Originally proposed in [21], under certain assumptions that will be discussed later, this scheme enjoys several valuable properties, the most important one being the fact that it is *monotone*. As done before, we will limit ourselves to the case of electrons being the one related to holes treated in the same way.

The EAFE scheme can be viewed as a particular kind of Generalized Galerkin method, because it changes the bilinear form and the linear functional of the original variational problem, but leaves unaltered the discrete spaces (i.e. $X_h^1(\Omega_{Si})$). For the complete and detailed derivation of the scheme we refer to [21] and [23]; here we report only the following:

LEC - EAFE Formulation

Find $n_h \in X_h^1(\Omega_{Si}) \cap H^1_{\Gamma_{D,Si}}(\Omega_{Si})$ s.t.:

$$a_h^i(n_h^i, v_h) = L^i(v_h) \qquad \forall v_h \in X_h^1(\Omega_{Si}) \tag{2.27}$$

being $a_h^i(\cdot,\cdot)$ the EAFE bilinear form associated with problem (2.14) (see [21] for its definition) and L^i the linear functional defined as:

$$L^i(v) = \int_{\Omega_{Si}} f_n^i v \, d\Omega \,,$$

An advantage of this formulation comes from an implementation perspective: the functional space $X_h^1(\Omega_{Si})$ can be represented by a subset of the basis for $X_h^1(\Omega)$, hence, practically, just a single finite element space is required. Analogously for what done in the Nonlinear Poisson case, we can therefore exploit the usual hat function basis $\{\psi\}_{j=1}^{N_{h,Si}}$ to recover the algebraic formulation:

LEC - Algebraic Formulation

Find $\mathbf{n}^i \in \mathbb{R}^{N_{h,Si}}$ s.t.:

$$\mathbf{A}^i \mathbf{n}^i = \mathbf{b}^i \tag{2.28}$$

where $\mathbf{A}^i \in \mathbb{R}^{N_{h,Si} \times N_{h,Si}}$ and $\mathbf{b}^i \in \mathbb{R}^{N_{h,Si}}$ are defined as

$$[\mathbf{A}^i]_{i,j} = a_h^i(\psi_j, \psi_i)\,,$$
$$[\mathbf{b}^i]_i = L^i(\psi_i)\,.$$

It has been proven that, if the simplicial partition $\mathcal{T}_h$ satisfies a particular geometrical condition, the matrix obtained with the EAFE scheme, $\mathbf{A}^i$, is an M-matrix, hence the scheme is monotone and satisfies the *discrete maximum principle*. A similar result was already known for the 2D case, where the Delauny property has to be required for the triangulation. The generalization to the 3D case involves a more strict condition:

Theorem 2.1 (Zikatanov condition)**.** *The system matrix of the EAFE scheme is an M-matrix iff for any fixed edge E of the partition $\mathcal{T}_h$ the following inequality holds:*

$$\omega_E = \frac{1}{d(d-1)} \sum_{K \supset E} |k_E^K| cot\theta_E^K \geq 0, \tag{2.29}$$

where $\sum_{K \supset E}$ means summation over all simplices K containing E, θ_E^K is the angle between the faces f_i, $f_j \in \mathcal{T}_h$ such that $f_i \bigcap f_j = E$ and k_E^K is the edge in K which does not share any vertices with E.

Finally it has also been proven in [21], that such scheme converges to the exact solution of problem (2.15) with a linear rate with respect to the mesh size h.

2.4 Time Discretization

In this section we present time discretization schemes and we discuss how to combine them with the Gummel map framework in order to deal with a time dependent Drift-Diffusion model.

2.4.1 One-step methods

Let us consider the generic initial value problem (IVP) for $\mathbf{y} : \mathbb{R} \mapsto \mathbb{R}^n$:

$$\begin{cases} \dfrac{d}{dt}\mathbf{y}(t) = \mathbf{f}(t, \mathbf{y}(t)), & t \in I = (t_0, t_0 + T) \\ \mathbf{y}(0) = \mathbf{y}_0 \end{cases} \tag{2.30}$$

where $T > 0$ (possibly $T = +\infty$) and $\mathbf{f} : \mathbb{R} \times \mathbb{R}^n \mapsto \mathbb{R}^n$ is uniformly Lipschitz continuous in $\mathbf{y}$ and continuous in t, so that by the Picard-Lindelöf theorem, problem (2.30) admits a unique solution.

Let us now partition I into the sequence of subintervals $\{I_n = (t_{n-1}, t_n)\}_{n=1}^N$; we can then identify the set of discretization nodes or time levels, $\{t_n\}_{n=0}^N$, and the corresponding stepsizes $\{\Delta t_n = t_n - t_{n-1}\}_{n=1}^N$. Moreover, we indicate with $\mathbf{u}_n$ the value of the discrete solution at time t_n (i.e., $\mathbf{u}_n = \mathbf{u}(t_n)$) and with $\mathbf{f}_n$ the evaluation $\mathbf{f}(t_n, \mathbf{u}_n)$.

One-step methods are a family of discretization schemes for IVPs that, in order to compute the value of $\mathbf{u}_{n+1}$, just employ the previous temporal solution, $\mathbf{u}_n$. Among these techniques, the best known is the Euler method, which simply prescribes that the time derivative is discretized as

$$\frac{d}{dt}\mathbf{y}(t) \approx \frac{\mathbf{y}(t + \Delta t) - \mathbf{y}(t)}{\Delta t} \tag{2.31}$$

which, thanks to (2.30), implies

$$\mathbf{y}(t + \Delta t) \approx \mathbf{y}(t) + \Delta t \mathbf{f}(t)$$

At a generic time level n, the value $\mathbf{u}_{n+1}$ can be therefore computed in two ways:

$$\text{(FE)} \qquad \mathbf{u}_{n+1} = \mathbf{u}_n + \Delta t_n \mathbf{f}_n \tag{2.32}$$

$$\text{(BE)} \qquad \mathbf{u}_{n+1} = \mathbf{u}_n + \Delta t_n \mathbf{f}_{n+1} \tag{2.33}$$

where, depending on the time level chosen for the evaluation of $\mathbf{f}$, the *explicit* Forward Euler method (FE) or the *implicit* Backward Euler (BE) are obtained. A more refined approach originates from the integration of (2.30) between t and $t + \Delta t$ as:

$$\mathbf{y}(t + \Delta t) = \mathbf{y}(t) + \int_t^{t+\Delta t} \mathbf{f}(s, \mathbf{y}(s))\, ds \tag{2.34}$$

from which we can notice that both of the two versions of Euler method can be recovered by approximating the integral with a left (FE) or right (BE)

endpoint integration rule. Evaluating the integral using the *trapezoidal rule* (2.34) becomes:

$$\begin{aligned}\mathbf{y}(t+\Delta t) &= \mathbf{y}(t) + \int_t^{t+\Delta t} \mathbf{f}(s, y(s))\, ds \\ &\approx \mathbf{y}(t) + \frac{\Delta t}{2}\left[\mathbf{f}(t+\Delta t, \mathbf{y}(t+\Delta t)) + f(t, \mathbf{y}(t))\right] ,\end{aligned}$$

thus leading to the *Crank-Nicolson* (or simply trapezoidal rule) method

$$\text{(TR)} \qquad \mathbf{u}_{n+1} = \mathbf{u}_n + \frac{\Delta t_n}{2}\left[\mathbf{f}_{n+1} + \mathbf{f}_n\right] . \tag{2.35}$$

A convenient way to express all of these three time discretization schemes in a more compact manner is the θ-method:

$$(\theta\text{-method}) \qquad \frac{\mathbf{u}_{n+1} - \mathbf{u}_n}{\Delta t_n} = \theta \mathbf{f}_{n+1} + (1-\theta)\mathbf{f}_n \tag{2.36}$$

with $\theta \in [0, 1]$. It can be immediately noticed that for $\theta = 0, 1, \frac{1}{2}$ we obtain the FE, BE and TR methods, respectively.

As far as the numerical properties of these three methods are concerned, both FE and BE converge with a linear rate $\mathcal{O}(\Delta t)$, while the TR scheme attains a better result being $\mathcal{O}(\Delta t^2)$ accurate. Regarding stability, instead, BE and TR are A-stable, while FE is only conditionally stable. The BE method is the only one that is also L-stable. These facts suggest that the most suitable time discretization for the D.D. model is the BE scheme.

2.4.2 The TRBDF2 Scheme

The TRBDF2 method is a composite scheme proposed in [2], which combines the trapezoidal rule (TR) and the second order Backward Difference Formula (BDF2) in a two-step method. The rationale behind this coupling is to simultaneously get the accuracy of the trapozoidal rule while keeping the good stability properties of the BDF2 scheme. To obtain the BDF2 method we need to start from (2.30) and directly approximate the value of the first derivative of $\mathbf{y}$ at node t_{n+1} with the first derivative of the piecewise linear polynomial interpolating $\mathbf{y}$ at nodes t_{n+1}, t_n and t_{n-1}:

$$\begin{aligned}\mathbf{p}(s) = \mathbf{y}(t_{n+1}) + (s - t_{n+1})\, \frac{\mathbf{y}(t_{n+1}) - \mathbf{y}(t_n)}{\Delta t} + \\ (s - t_n)\, \frac{\mathbf{y}(t_{n+1}) - 2\mathbf{y}(t_n) + \mathbf{y}(t_{n-1})}{2\Delta t}\end{aligned}$$

whose derivative at t_{n+1} is

$$\mathbf{p}'(t_{n+1}) = \frac{3\mathbf{y}(t_{n+1}) - 4\mathbf{y}(t_n) + \mathbf{y}(t_{n-1})}{2\Delta t}\,.$$

In (2.30) we approximate the derivative of $\mathbf{y}$ at time t_{n+1} with $\mathbf{p}'(t_{n+1})$

$$\frac{3\mathbf{y}(t_{n+1}) - 4\mathbf{y}(t_n) + \mathbf{y}(t_{n-1})}{2\Delta t} = \mathbf{f}(t_{n+1})\,,$$

and expliciting $\mathbf{y}(t_{n+1})$ we obtain

$$\mathbf{y}(t_{n+1}) = \frac{4}{3}\mathbf{y}(t_n) - \frac{1}{3}\mathbf{y}(t_{n-1}) + \frac{2\Delta t}{3}\mathbf{f}(t_{n+1})\,.$$

This motivates the second order Backward Difference Formula:

$$\text{(BDF2)} \qquad \mathbf{u}_{n+1} = \frac{4}{3}\mathbf{u}_n - \frac{1}{3}\mathbf{u}_{n-1} + \frac{2\Delta t}{3}\mathbf{f}_{n+1}\,. \tag{2.37}$$

This method is both A-stable and L-stable, moreover it has a convergence rate of $\mathcal{O}(\Delta t^2)$. The way in which the TRBDF2 scheme arranges the two methods is then the following: starting from t_n, an intermediate solution at time level $t_{n+\gamma}$ with $\gamma \in (0,1)$ is computed using the trapezoidal rule:

$$\mathbf{u}_{n+\gamma} - \frac{\gamma}{2}\Delta t_n \mathbf{f}_{n+\gamma} = \mathbf{u}_n + \frac{\gamma}{2}\Delta t_n \mathbf{f}_n\,. \tag{2.38}$$

Afterwards, the algorithm marches to the timestep t_{n+1} using the BDF2 scheme:

$$\mathbf{u}_{n+1} - \frac{1-\gamma}{2-\gamma}\Delta t_n \mathbf{f}_{n+1} = \frac{1}{\gamma(2-\gamma)}\mathbf{u}_{n+\gamma} - \frac{(1-\gamma)^2}{\gamma(2-\gamma)}\mathbf{u}_n\,. \tag{2.39}$$

Except for being sufficiently regular, no other assumption has been made on $\mathbf{f}$, that can be a generic nonlinear function. An iterative method is hence required to solve these two steps. In view of applying the Newton method we set

$$\begin{cases} \mathbf{u}^{k+1}_{n+\gamma} = \mathbf{u}^k_{n+\gamma} + \delta\mathbf{u}^k_{n+\gamma} \\ \mathbf{u}^0_{n+\gamma} = \mathbf{u}_n \end{cases} \qquad \begin{cases} \mathbf{u}^{k+1}_{n+1} = \mathbf{u}^k_{n+1} + \delta\mathbf{u}^k_{n+1} \\ \mathbf{u}^0_{n+1} = \mathbf{u}_{n+\gamma} \end{cases}$$

where k is the Newton iteration index. The equation for the linearized TR substep is then

$$\left[1 - \frac{\gamma\Delta t_n}{2}\left(\frac{\partial \mathbf{f}}{\partial \mathbf{u}}\right)^k_{n+\gamma}\right]\delta\mathbf{u}^k_{n+\gamma} = -(\mathbf{u}^k_{n+\gamma} - \mathbf{u}_n) + \frac{\gamma\Delta t_n}{2}(\mathbf{f}^k_{n+\gamma} + \mathbf{f}_n)\,, \tag{2.40}$$

while the one for the BDF2 reads as

$$\left[1-\frac{1-\gamma}{2-\gamma}\Delta t_n\left(\frac{\partial \mathbf{f}}{\partial \mathbf{u}}\right)^k_{n+1}\right]\delta\mathbf{u}^k_{n+1} = \\ -\left[\mathbf{u}^k_{n+1}-\frac{1}{\gamma(2-\gamma)}\mathbf{u}^k_{n+\gamma}+\frac{(1-\gamma)^2}{\gamma(2-\gamma)}\mathbf{u}_n\right]+\frac{1-\gamma}{2-\gamma}\Delta t_n\mathbf{f}^k_{n+1}\,. \tag{2.41}$$

Furthermore, it is worth noticing that the Jacobian matrices for these two substeps are:

$$\mathbf{J}_{TR}=\mathbf{I}-\frac{\gamma\Delta t_n}{2}\left(\frac{\partial \mathbf{f}}{\partial \mathbf{u}}\right)^k_{n+\gamma}\,, \qquad \mathbf{J}_{BDF2}=\mathbf{I}-\frac{1-\gamma}{2-\gamma}\Delta t_n\left(\frac{\partial \mathbf{f}}{\partial \mathbf{u}}\right)^k_{n+1}\,.$$

Requiring them to be equal and solving for the parameter γ, we find:

$$\gamma^* = 2-\sqrt{2} \tag{2.42}$$

which can be considered optimal, in the sense that for this particular value, not only the computational effort is reduced (a single Jacobian matrix has to be inverted), but also the method is L-stable and the local truncation error (LTE) is minimized [2].

2.4.3 Time-dependent Gummel map

The way to take into account the time dependency follows a very natural idea: provided a suitable initial guess, (φ_0, n_0, p_0), the discrete solution at a certain instant t_n is marched towards t_{n+1} by solving a modified version of the Gummel map algorithm, in which the linearized continuity equations embed a proper time-advancement scheme. The Nonlinear Poisson solving procedure, instead, remains unchanged. The overall procedure can be synthetically outlined as in Algorithm 2, where for each quantity involved we have indicated with the subscript j the time level (for avoiding confusion with the electron density n) and with the superscript i the Gummel map iteration counter. The inclusion of the time derivative implies the construction of a new weak formulation for the LEC equation. With this aim, we multiply equation (2.8) by a test function $v \in V = H^1_{\Gamma_{D,Si}}(\Omega_{Si})$ to obtain:

$$\langle \partial_t n, v\rangle_* + a^i(n,v) = L^i(v)$$

where $a(\,\cdot\,,\,\cdot\,)$ and $L^i(\,\cdot\,)$ are the same as in (2.15), while $\langle\,\cdot\,,\,\cdot\,\rangle_*$ indicates the duality between V and its topological dual space V^*. We can give to the

Algorithm 2: Time-dependent Gummel Map

Input:
φ_0, electrostatic potential initial condition;
n_0, electron density initial condition;
p_0, hole density initial condition;
T, ending time;
Δt_0, initial stepsize;
tol_{NLP}, Nonlinear Poisson tolerance;
tol_{GM}, Gummel Map tolerance;

$t = 0$ $\Delta t = \Delta t_0$
$j = 0$
while $t < T$ **do**
  $t = t + \Delta t$
  $i = 0$
  $tol = \infty$
  while $tol \geq tol_{GM}$ **do**
    $i = i + 1$
    φ_n^{i-1}, $\varphi_p^{i-1} \leftarrow$ compute quasi-Fermi potential(n_j^{i-1}, p_j^{i-1})
    $\varphi_j^i \leftarrow$ solve NLP$(\varphi_j^{i-1}, \varphi_n^{i-1}, \varphi_p^{i-1}, tol_{NLP})$
    $n_j^i \leftarrow$ solve LEC$(\varphi_j^i, n_j^{i-1}, p_j^{i-1}, \varphi_{j-1}, n_{j-1}, p_{j-1})$
    $p_j^i \leftarrow$ solve LHC$(\varphi_j^i, n_j^{i-1}, p_j^{i-1}, \varphi_{j-1}, n_{j-1}, p_{j-1})$
    $tol \leftarrow$ compute GM tolerance$(n^i, p^i, n^{i-1}, p^{i-1})$
  end
  $\varphi_j = \varphi_j^i$
  $p_j = n_j^i$
  $n_j = p_j^i$
  $\Delta t \leftarrow$ compute timestep$(\dots)$
  $t = t + \Delta t$
  $j = j + 1$
end

latter one a more explicit expression recalling that, in a distributional sense (see [16])

$$\langle \partial_t n, v \rangle_* = \frac{d}{dt}(n(t), v)_0 \tag{2.43}$$

$(\,\cdot\,,\,\cdot\,)_0$ being the inner product on $L^2(\Omega_{Si})$. For our implementation purposes, we focus on the Backward Euler scheme and approximate the time derivative as in (2.33) to obtain

$$\frac{1}{\Delta t}\left(n^i_{j+1} - n_j, v\right)_0 + a^i(n_{j+1}, v) = L^i(v) \tag{2.44}$$

so that the fully-discretized EAFE formulation can be recovered

BE-LEC - EAFE Formulation

Find $n^i_{h,j+1} \in X^1_h(\Omega_{Si}) \cap H^1_{\Gamma_{D,Si}}(\Omega_{Si})$ s.t.:

$$\frac{1}{\Delta t}\left(n^i_{h,j+1} - n_{h,j}, v\right)_0 + a^i_h(n^i_{h,j+1}, v_h) = L^i(v_h) \qquad \forall v_h \in X^1_h(\Omega_{Si}) \tag{2.45}$$

Even though this formulation is slightly different from the one associated with the stationary problem (2.15), it can be treated in the same way: the effect of the time discretization just adds a reaction term that can be included in the one already present. Moreover, exploiting again the Lagrangian basis $\{\psi_l\}_{i=1}^{N_h,Si}$ we are able to recover the algebraic counterpart of (2.45):

BE-LEC - Algebraic Formulation

Find $\mathbf{n}^i_{j+1} \in \mathbb{R}^{N_{h,Si}}$ s.t.:

$$\left(\frac{1}{\Delta t}\mathbf{M} + \mathbf{A}^i\right)\mathbf{n}^i_{j+1} = \mathbf{b}^i + \frac{1}{\Delta t}\mathbf{M}\mathbf{n}_j \tag{2.46}$$

where $\mathbf{A}^i \in \mathbb{R}^{N_{h,Si}\times N_{h,Si}}$ and $\mathbf{b}^i \in \mathbb{R}^{N_{h,Si}}$ are defined as

$$\begin{aligned}[\mathbf{M}]_{i,j} &= (\psi_j, \psi_i)_0\,,\\ [\mathbf{A}^i]_{i,j} &= a^i_h(\psi_j, \psi_i)\,,\\ [\mathbf{b}^i]_i &= L^i(\psi_i)\,.\end{aligned}$$

where $\mathbf{M}$ is the *mass-matrix* originating from the time discretization and boundary conditions are enforced by means of the diagonalization technique applied to the global system matrix

$$\overline{\mathbf{A}}^i = \frac{1}{\Delta t}\mathbf{M} + \mathbf{A}^i\,. \tag{2.47}$$

The TRBDF2 scheme is slightly more complex to treat because it involves two steps, but the mathematical procedure needed to retrieve its associated EAFE formulation is exactly the same. Moreover, it is worth pointing out that we consider the *linearized* continuity equations, so that Newton's method is not required and a direct solving approach is possible. Introducing the weak residual of (2.27)

$$r^i(u_h, v_h) = L^i(v_h) - a_h^i(u_h, v_h)\,,$$

and indicating with r_j the residual at the previously converged time level j, we can state the EAFE formulations for the two substeps of the TRBDF2 scheme as follows:

TRBDF2-LEC - EAFE Formulation

TR substep

Find $n^i_{h,j+\gamma} \in X^1_h(\Omega_{Si}) \cap H^1_{\Gamma_{D,Si}}(\Omega_{Si})$ s.t.:

$$\begin{aligned} &\left(n^i_{h,j+\gamma}, v\right)_0 - \frac{\gamma\Delta t}{2}\, r^i(n^i_{h,j+\gamma}, v_h) \\ &= (n_{h,j}, v)_0 + \frac{\gamma\Delta t}{2}\, r_j(n_{h,j}, v_h) \qquad \forall v_h \in X^1_h(\Omega_{Si}) \end{aligned} \tag{2.48}$$

BDF2 substep

Find $n^i_{h,j+1} \in X^1_h(\Omega_{Si}) \cap H^1_{\Gamma_{D,Si}}(\Omega_{Si})$ s.t.:

$$\begin{aligned} &\left(n^i_{h,j+1}, v\right)_0 - \frac{1-\gamma}{2-\gamma}\Delta t\, r^i(n^i_{h,j+1}, v_h) \\ &= \frac{1}{\gamma(2-\gamma)}\left(n^i_{h,j+\gamma}, v\right)_0 - \frac{(1-\gamma)^2}{\gamma(2-\gamma)}\,(n_{h,j}, v)_0 \qquad \forall v_h \in X^1_h(\Omega_{Si}) \end{aligned} \tag{2.49}$$

Using the usual finite element space basis, it is possible to retrieve the corresponding algebraic quantities. As done in (2.46), we set

$$\begin{aligned} [\mathbf{M}]_{i,j} &= (\psi_j, \psi_i)_0\,, \\ [\mathbf{A}^i]_{i,j} &= a^i_h(\psi_j, \psi_i)\,, \\ [\mathbf{b}^i]_i &= L^i(\psi_i)\,. \end{aligned}$$

Moreover we define $\mathbf{A}_j$ and $\mathbf{b}_j$ to be the EAFE matrix and the right-hand side of the previous time level j, respectively. We can therefore proceed in providing the algebraic formulation for the TRBDF2 discretization:

TRBDF2-LEC - Algebraic Formulation

TR substep

Find $\mathbf{n}^i_{j+\gamma} \in \mathbb{R}^{N_{h,Si}}$ s.t.:

$$\left(\frac{2}{\gamma\Delta t}\mathbf{M} + \mathbf{A}^i\right)\mathbf{n}^i_{j+\gamma} = \left(\mathbf{b}^i + \mathbf{b}_j\right) + \left(\frac{2}{\gamma\Delta t}\mathbf{M} - \mathbf{A}_j\right)\mathbf{n}_j \tag{2.50}$$

BDF2 substep

Find $\mathbf{n}^i_{j+1} \in \mathbb{R}^{N_{h,Si}}$ s.t.:

$$\left(\frac{2-\gamma}{(1-\gamma)\Delta t}\mathbf{M} + \mathbf{A}^i\right)\mathbf{n}^i_{j+1} = \mathbf{b}^i + \frac{1}{\gamma(1-\gamma)\Delta t}\mathbf{M}\mathbf{n}^i_{j+\gamma} - \frac{1-\gamma}{\gamma\Delta t}\mathbf{M}\mathbf{n}_j \tag{2.51}$$

Chapter 3

Stationary Drift-Diffusion Model: Simulation Results

This chapter is devoted to illustrating the results obtained by numerically solving the stationary Drift-Diffusion system (1.40)-(1.50) for both an n-channel and a p-channel MOSFET using FEMOS-MP, a C++ code that implements all of the numerical techniques and physical models described in Chapt. 1 and Chapt. 2.
In the first part, we analyze the behaviour of the devices in forward bias conditions, with particular attention to, the body effect and the temperature dependence, whereas the last section is dedicated to the study of the reverse bias regime.

3.1 Forward Bias

The geometry and mesh of the considered structure are shared by both the n-channel and the p-channel MOSFET and are shown in Fig. 3.1: the bulk region is 300 nm long, 270 nm and 40 nm thick, while the top oxide layer is 30 nm thick. The channel length is approximately 40 nm.

Material	**Width**	**Height**	**Thickness**	ϵ_r
Silicon	300 nm	40 nm	270 nm	11.6
Oxide	230 nm	40 nm	30 nm	3.9

Table 3.1: MOSFET geometry and parameters

To reproduce a realistic n-MOSFET, a p-substrate with a Boron acceptor concentration of $1 \times 10^{17}\,\mathrm{cm}^{-3}$ has been implanted with Arsenic and Phos-

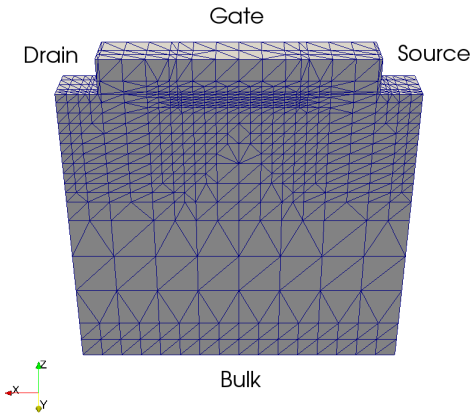

Figure 3.1: Device Geometry and Mesh

phorous ions to generate, respectively, the source and drain regions. In both cases, the donor concentrations are given by an analytic Gaussian profile with a peak of $\sim 1 \times 10^{18}\,\mathrm{cm}^{-3}$ at the corresponding contact and vanishing as going towards the bottom surface (bulk contact) as can be seen in Fig. 3.2a. Analogously, the p-MOSFET has a Phosphorous based n-substrate in which Boron ions have been implanted in both the source and drain regions, again following a Gaussian profile (Fig. 3.2b).

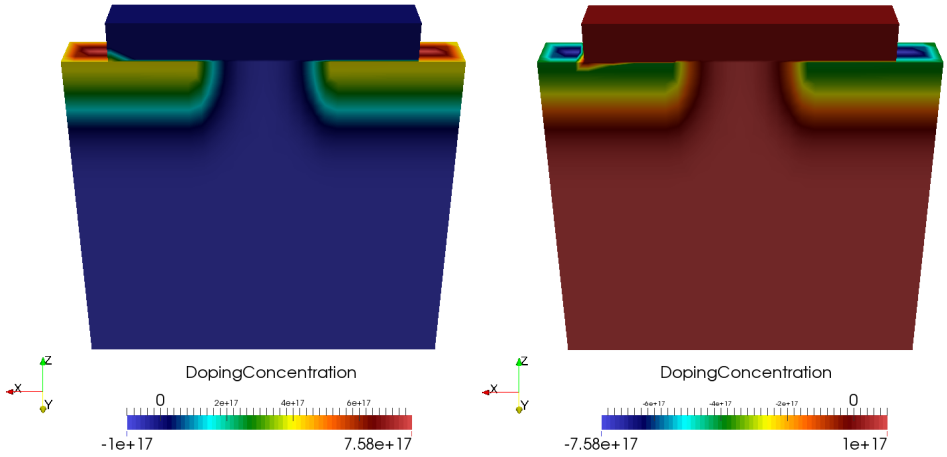

(a) n-MOSFET Doping **(b)** p-MOSFET Doping

Figure 3.2: Doping profiles

To assess the validity of the EAFE scheme combined with the Gummel map decoupling algorithm, the aforementioned MOSFETs have been analyzed in various bias conditions. For reading benefits, the results obtained

with FEMOS-MP have been compared with the ones provided by the commercial tool [1].
The $I_D - V_G$ characteristics for the n-channel device and $I_S - V_G$ for the p-channel one are reported, respectively, in Fig. 3.3a and Fig. 3.3b. In each of these simulations, the mobility has been calculated using the low-field Masetti model combined with the high-field Canali model (the driving force has been set equal to the gradient of the quasi-Fermi potential), while carrier R/G is taken into account by activating Shockley-Read-Hall and Auger mechanisms. Moreover, the devices are considered having a uniform constant temperature of 300 K. Tab. 3.2 and Tab. 3.3 summarize the contact biases and the physical models activated for both transistor types.

V_D [V]	V_G [V]	R/G Models	Mobility Models
0.1, 0.2, 0.5, 1.0	$-0.5 \div 1.5$	SRH, Auger	Masetti Canali (QF)

Table 3.2: Forward bias - n-MOSFET simulation settings

V_S [V]	V_G [V]	R/G Models	Mobility Models
0.01, 0.02, 0.1, 0.2, 0.5	$0.5 \div -1.5$	SRH, Auger	Masetti Canali (QF)

Table 3.3: Forward bias - p-MOSFET simulation settings

The agreement with the reference software is evident: in most cases the two results match perfectly, just showing a little discrepancy under the most intense working conditions.
Considering the n-MOSFET, as the gate terminal bias increases, electrons start to accumulate right next to the oxide interface (substrate inversion). This leads to the channel formation and brings the transistor in an on-state, as shown in Fig. 3.4. The p-MOSFET case is analogous, but the mechanism is actuated by holes (Fig. 3.5).
Snapshots for current densities streamlines are provided for both devices in Fig. 3.6: in the n-MOSFET case we have set $V_D = 0.1$V, $V_G = 1.5$V, while for the p-MOSFET we have considered $V_S = 0.1$V, $V_G = -1.5$V. As expected, most of the current carried by the transistors flows in a small section adjacent to the oxide layer. The computation has been performed using method A proposed in [14].

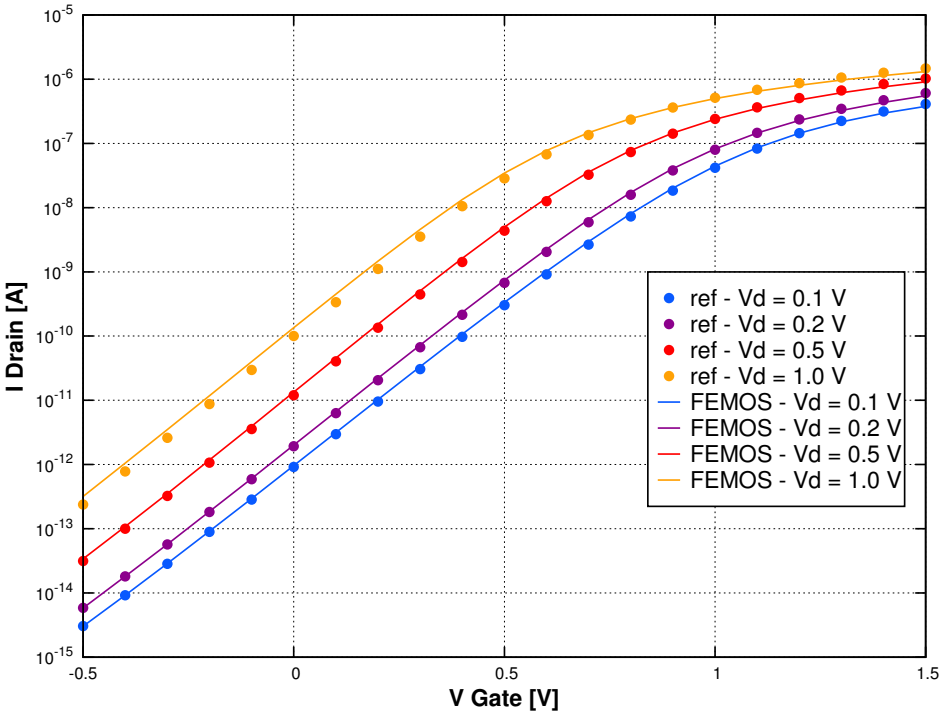

(a) n-MOSFET I_D-V_G

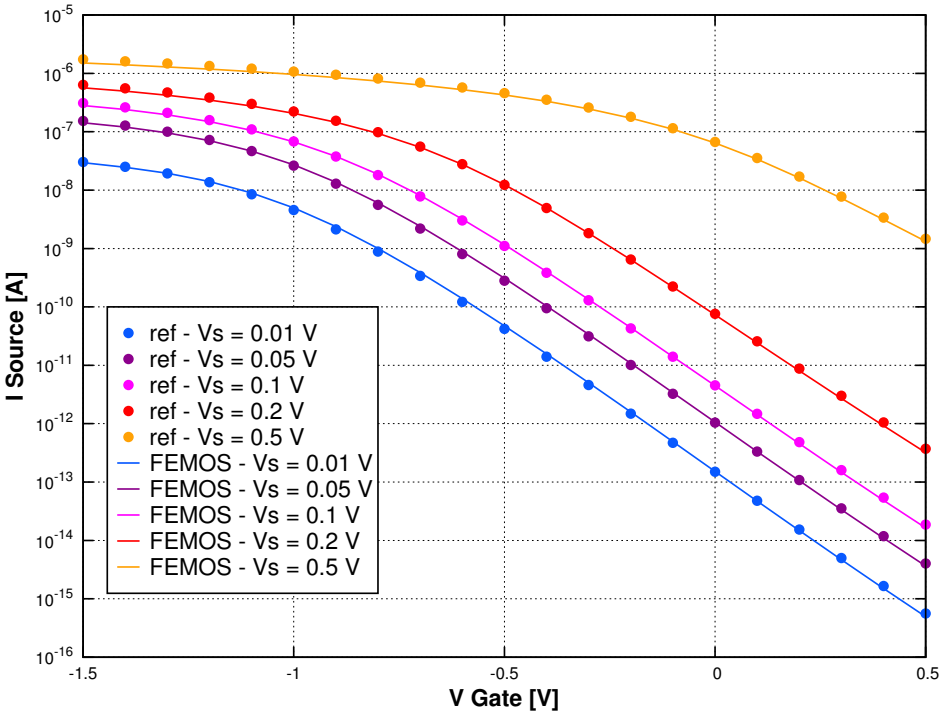

(b) p-MOSFET I_S-V_G

Figure 3.3: MOSFET forward bias: comparison between FEMOS (lines) and ref [1] (dots).

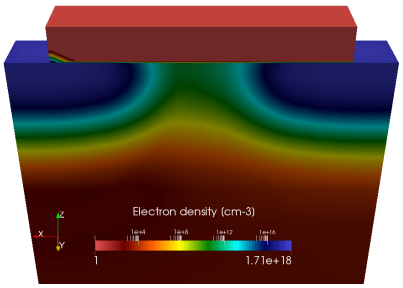

(a) $V_G = 0.0\,\mathrm{V}$

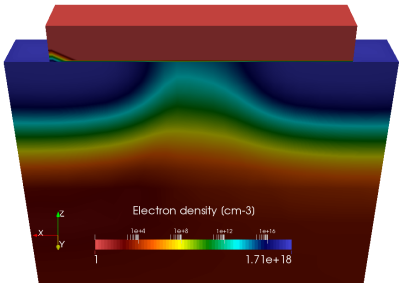

(b) $V_G = 0.5\,\mathrm{V}$

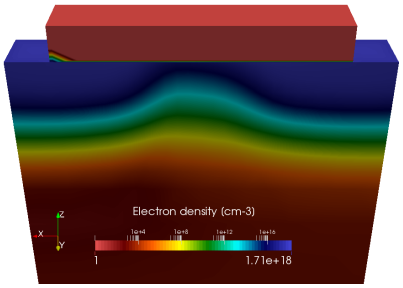

(c) $V_G = 1.0\,\mathrm{V}$

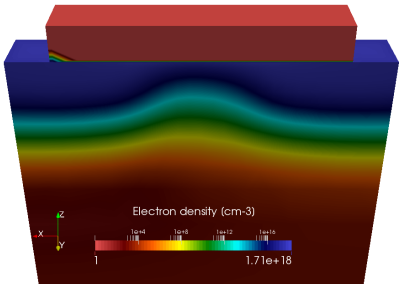

(d) $V_G = 1.5\,\mathrm{V}$

Figure 3.4: n-MOS channel formation - electron density for $V_D = 0.1\,\mathrm{V}$ and different gate voltages.

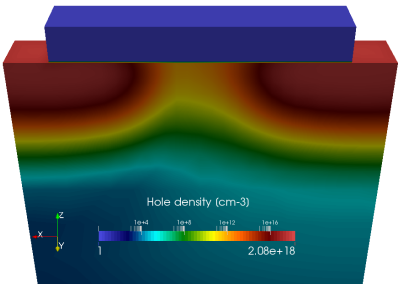

(a) $V_G = 0.0\,\mathrm{V}$

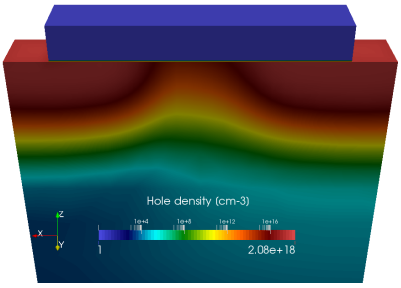

(b) $V_G = -0.5\,\mathrm{V}$

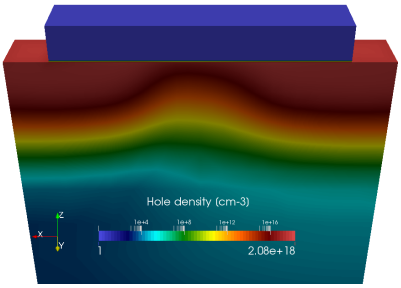

(c) $V_G = -1.0\,\mathrm{V}$

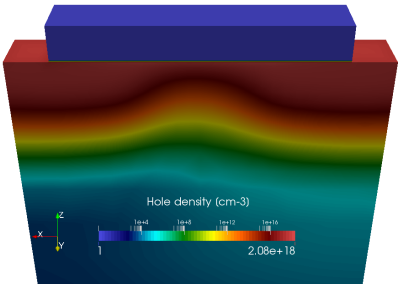

(d) $V_G = -1.5\,\mathrm{V}$

Figure 3.5: p-MOS channel formation - hole density for $V_S = 0.1\,\mathrm{V}$ and different gate voltages.

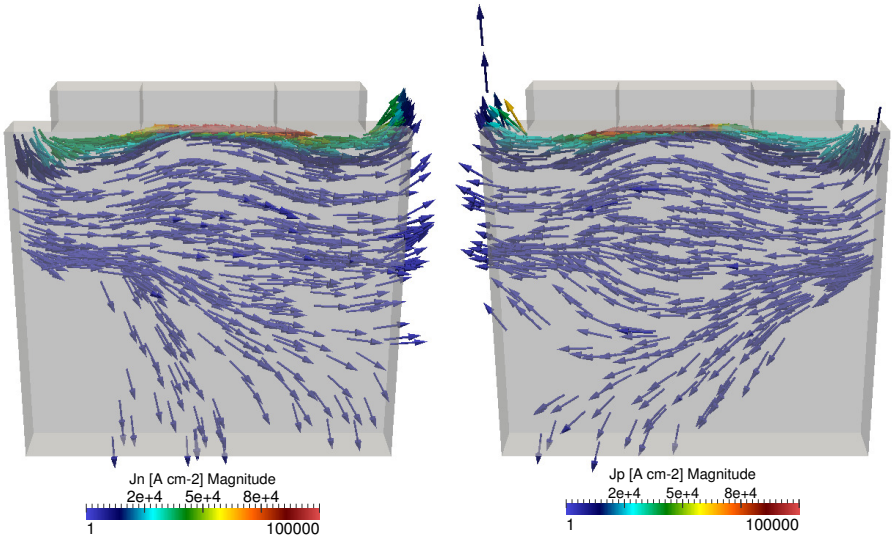

(a) n-MOSFET - $\mathbf{J}_n$ **(b)** p-MOSFET - $\mathbf{J}_p$

Figure 3.6: Current density streamlines.

3.2 Mobility Analysis

In the previous section, the $I-V$ characteristics have been calculated activating all of the mobility models available. The following *a posteriori* analysis has the purpose of proving the correctness of such choice or, equivalently, to estabilish that in order to obtain reliable predictions none of the considered mechanisms can be neglected. To do so, we have considered an n-MOSFET with a fixed drain voltage of 1 V and ramped up the gate bias from -0.5 V to 1.5 V (see Tab. 3.4). We have performed a simulation for each possi-

V_G [V]	V_D [V]	Mobility Models	R/G Models
$-0.5 \div 1.5$	1.0	$\mu_n = 1417\,\mathrm{cm^2V^{-1}s^{-1}}$ $\mu_p = 470.5\,\mathrm{cm^2V^{-1}s^{-1}}$	SRH, Auger
$-0.5 \div 1.5$	1.0	Masetti	SRH, Auger
$-0.5 \div 1.5$	1.0	Canali (QF)	SRH, Auger
$-0.5 \div 1.5$	1.0	Masetti, Canali (QF)	SRH, Auger

Table 3.4: Mobility analysis - simulation settings

ble combination of the implemented models and collected the results in Fig. 3.7. It can be immediately noticed that the constant mobility assumption is

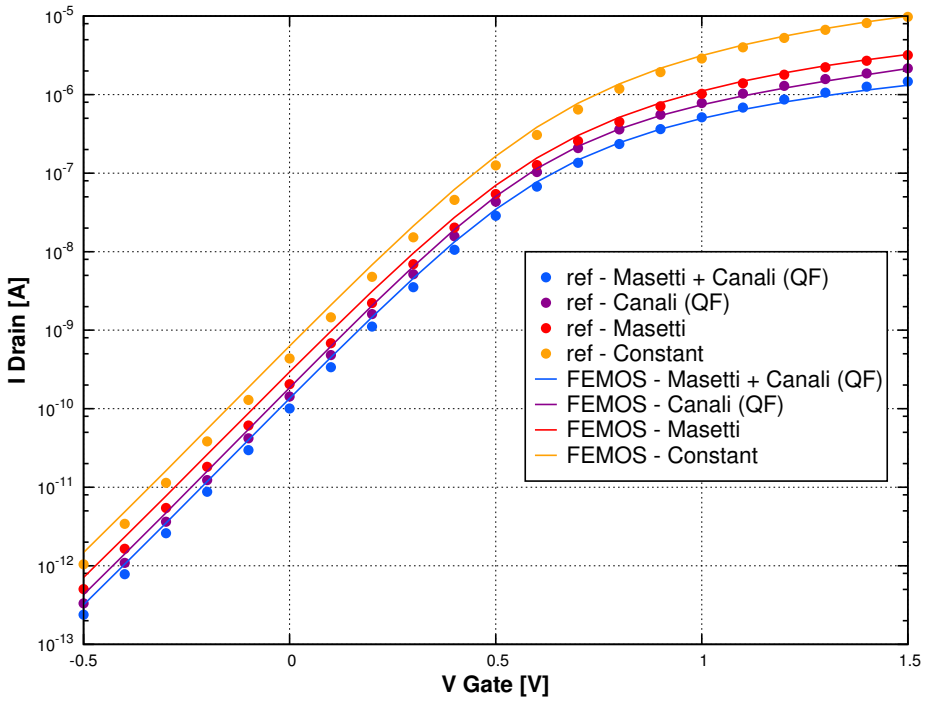

Figure 3.7: n-MOSFET mobility analysis: $I_D - V_G$ comparison between FEMOS (lines) and ref. [1] (dots)

uncapable to provide a meaningful output: the introduction of either the ionized impurities scattering phenomenon (Masetti) or the high-field mobility degradation (Canali) induces a significant lowering of the maximum current density. Activating both of the two physical mechanisms results in a further decrease of the current peak value, indicating that none of these effects can be left out.

As regards the comparison with the reference tool, the agreement is enough satisfactory considering the rather intense bias applied: a few differences are present in the subtreshold region, but almost vanish as approching saturation condition.

For completeness, in Fig. 3.8 we show the $I - V$ characteristics obtained using different driving forces for the high-field model computation: at this level a discrepancy exists, but is barely perceivable.

A more interesting comparison is instead reported in Fig. 3.9, that illustrates various 3D representations of the electron mobility throughout the device. As expected, switching on the Masetti model will results in a great

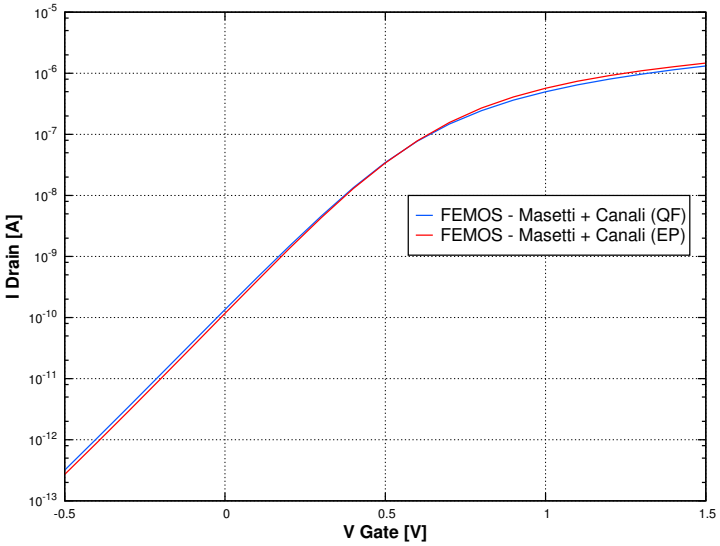

Figure 3.8: Mobility comparison - $I_D - V_G$ for different driving forces used in the Canali model computation

.

specular reduction within the highly doped source and drain regions and a lesser, albeit still consistent, cut-off in the substrate (Fig. 3.9a). In contrast with that, the Canali model (Fig. 3.9b) exhibits an unsymmetric behaviour: the most interested device region is the one closer to the drain terminal, where the external bias is applied and the device is far away from the equilibrium. In this latter case, is it worth noticing that the mobility is highly reduced in the region occupied by the channel, thus having a greater impact in decresing the contact current. This fact can be verified in Fig. 3.7, where the peak value attained is lower than the one associated with the activation of the sole scattering from ionized impurities. Finally, the results obtained employing the two models are supplied in Fig. 3.9c and 3.9d: the mobility calculated using the quasi-Fermi potential driving force (QF) seems to be more homogeneous than the one computed with the parallel electric field approach (EP).

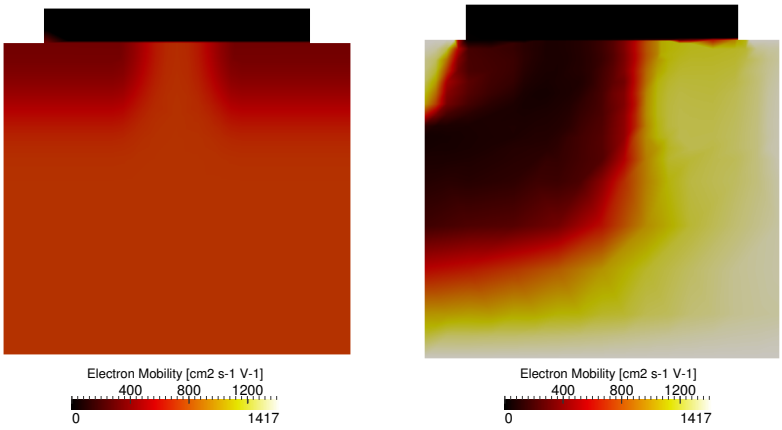

(a) Masetti **(b)** Canali (QF)

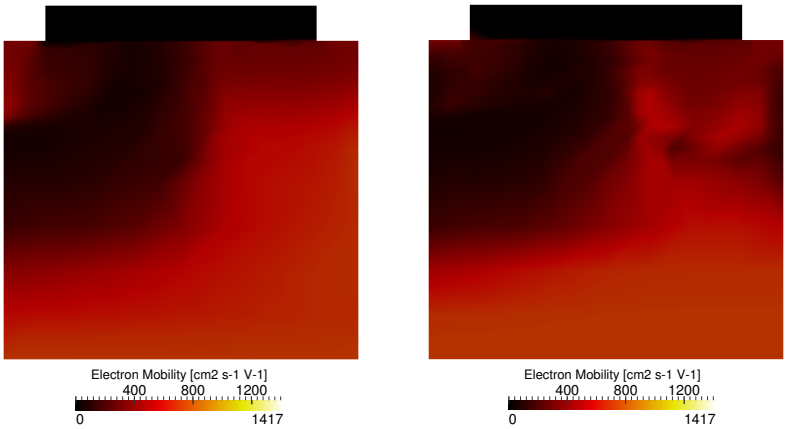

(c) Masetti + Canali (QF) **(d)** Masetti + Canali (EP)

Figure 3.9: Electron mobility for different models activated at $V_D = 1\,\mathrm{V}$ and $V_G = 1.5\,\mathrm{V}$.

3.3 Body Effect

For practical reasons, in transistors composing integrated circuits source contacts are grounded, but not connected to the substrate body which is instead left in a"floating" state, thus allowing a voltage drop between the two terminals to occur. The existence of a non-zero bulk-to-source potential difference V_{BS} is responsible for inducing a modification to the threshold voltage V_T. From a theoretical standpoint, the following expression for V_T can be obtained for a p-substrate [22]:

$$V_T = V_{fb} + \psi_s + \frac{\sqrt{2\varepsilon_{si} q N_a (\psi_s - V_{BS})}}{C_{ox}} \tag{3.1}$$

where V_{fb} is the flatband potential [V], ψ_s is the surface potential [V] and C_{ox} is the oxide specific capacitance [$\mathrm{F\,m^{-2}}$]. Even though this formula cannot be directly applied to obtain accurate results in modern devices, it highlights the fact that the consequence of a forward substrate bias is to reduce the bulk depletion region and decrease the threshold voltage. For this reason, such behaviour is commonly known as body or back-gate effect.
To numerically observe this phenomenon, we have performed a few simulations considering an n-MOSFET and fixing everything but the body bias, as indicated in Tab. 3.5.

V_B [V]	V_G [V]	V_D [V]	R/G Models	Mobility Models
0.0, 0.1, 0.25, 0.5	$-0.5 \div 1.5$	0.1	SRH, Auger	Masetti Canali (QF)

Table 3.5: Body effect study - simulation settings

The results are illustrated in Fig. 3.10: the obtained values are coherent with both the theoretical intuition and the reference tool. The threshold voltage is subjected to an increase as the potential applied to the body contact grows, as predicted by equation (3.1). At the same time, the subtrhreshold slope (STS) becomes slighly less steep, consequentially raising the leakage current value (substrate sensitivity). The extreme scenario is represented by the characteristic related to the 0.5 V bias (yellow line in Fig.3.10), where off-state current is four order of magnitude greater than in the unbiased case.

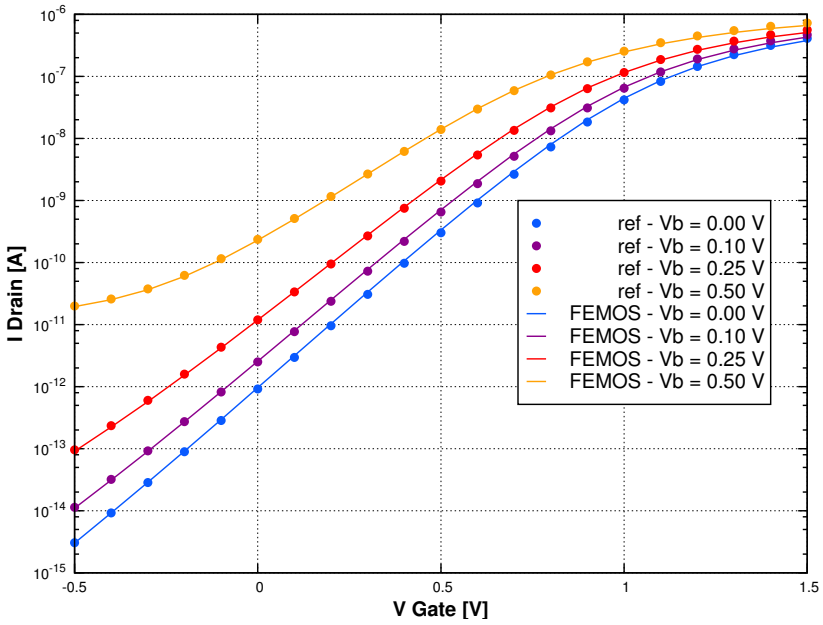

Figure 3.10: n-MOSFET body effect study: $I_D - V_G$ comparison between FEMOS (lines) and ref. [1] (dots).

3.4 Temperature Dependence

As pointed out in Sect. 1.3, many of the quantities involved in the simulation of a semiconductor device are affected by temperature. In the following we consider the thermal dependence of model solution through a uniform constant temperature that assumes a few values covering the typical operational range required in automotive applications, $-40\,°\mathrm{C}$ to $125\,°\mathrm{C}$. As previously done, all of the mobility models available are activated (i.e. Masetti an Canali with the quasi-Fermi gradient driving force), as well as the Shockley-Read-Hall and Auger R/G mechanisms. The temperature dependent phenomena include the phonon scattering (1.57), the bandgap narrowing (1.73) and the density of states modification (1.79)-(1.81). These latter ones are summarized in Tab. 3.6, together with the employed biases.

The results are reported in Fig. 3.12a for the n-MOSFET and Fig. 3.12b for the p-MOSFET. As temperature grows, the current flowing in both devices increases in the subthreshold region. Two are the main causes:

- the additional heat increases the value of the effective intrinsic concentration n_i;
- the energy bandgap gets reduced.

T [°C]	V_G [V]	V_D [V]	Temperature Dependence Models
-40, 26.85, 85, 125	$-0.5 \div 1.5$	0.1	Lattice Scattering Bandgap Narrowing Intrinsic concentration

Table 3.6: Temperature dependence analysis - n-MOSFET simulation settings

T [°C]	V_G [V]	V_S [V]	Temperature Dependence Models
-40, 26.85, 85, 125	$0.5 \div -1.5$	0.1	Lattice Scattering Bandgap Narrowing Intrinsic concentration

Table 3.7: Temperature dependence analysis - p-MOSFET simulation settings

These concurrent facts contribute in raising the number of available free carriers, hence the electric current.
On the contrary, as approaching the saturation condition, the current peak value is related to the temperature through an inversely proportional relationship: the reason is that the mobility decay caused by phonon scattering phenomena increase due to the silicon lattice being hotter, thus vibrating more. This effect is present for any bias condition, but it becomes immediately noticeable at high voltages (or rather for high electric field magnitude) because of the interaction with the carrier velocity saturation mechanism. Snapshots for the electron mobility in the n-MOSFET case are provided in Fig. 3.11a: albeit the shape of the two profiles is similar, the maximum value at $-40\,°\mathrm{C}$ (3.11a) is about four times greater than the one attained in the simulation performed at $125\,°\mathrm{C}$ (3.11b).

Another important quantity of interest affected by temperature is the threshold voltage. Using the Shichman-Hodges model, the following relationship can be derived for a n-channel transistor [22]:

$$\frac{d}{dT}V_T = -(2m-1)\frac{k_b}{q}\left[\ln\left(\frac{\sqrt{N_C N_V}}{N_A}\right)+\frac{3}{2}\right]+\frac{m-1}{q}\frac{d}{dT}E_g \tag{3.2}$$

where

$$m = 1+\frac{\sqrt{\varepsilon_{si} q N_a/4\psi_B}}{C_{ox}} \tag{3.3}$$

and where ψ_B is the bulk potential. Recalling the explicit expression (1.73) for E_g and (1.79) and (1.81) for the densities of states N_C, N_V , we can deduce

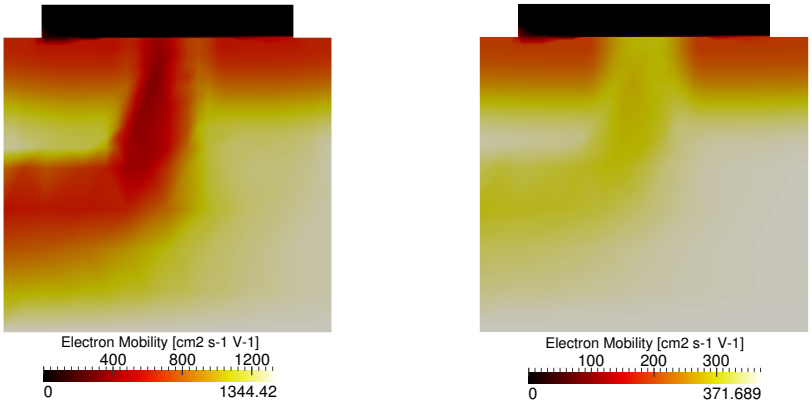

(a) $T = -40\,^{\circ}\mathrm{C}$ **(b)** $T = 125\,^{\circ}\mathrm{C}$

Figure 3.11: n-MOSFET - electron mobility at different temperatures

that to a temperature growth corresponds a threshold voltage decrease (it is easy to verify that both terms in (3.2) are positive quantities), which is in agreement with the output of our simulations. Moreover, a change in the subthreshold slope occurs: in the hottest case (125 °C) the STS is significantly less steep than the one associated with the simulations performed at lower temperature, thus implying a raise of the leakage current and a degradation in the transistor off-state performance.

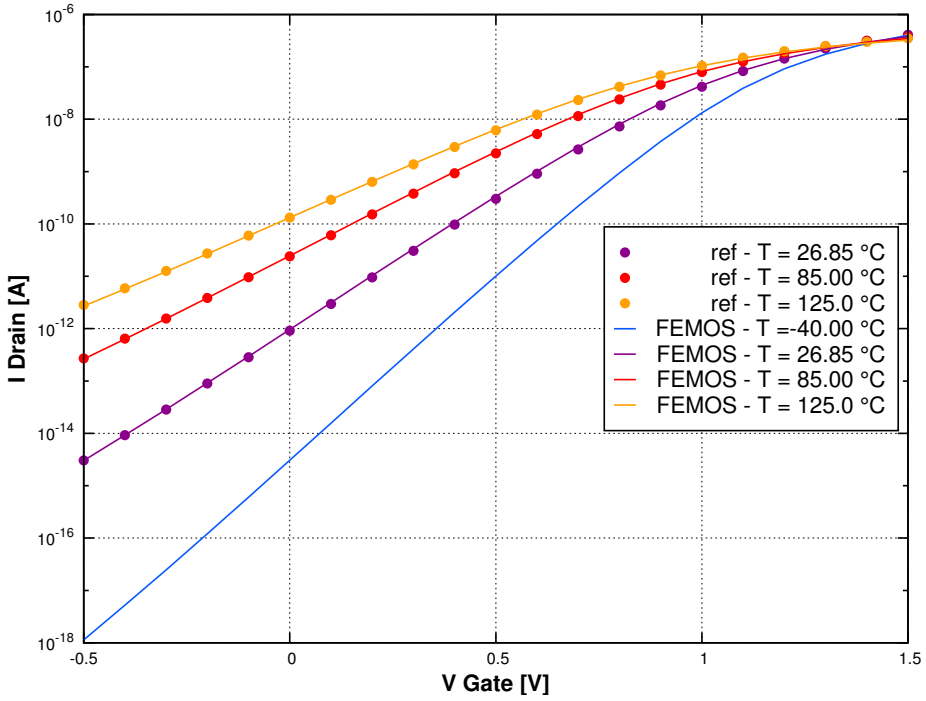

(a) n-MOSFET I_D-V_G

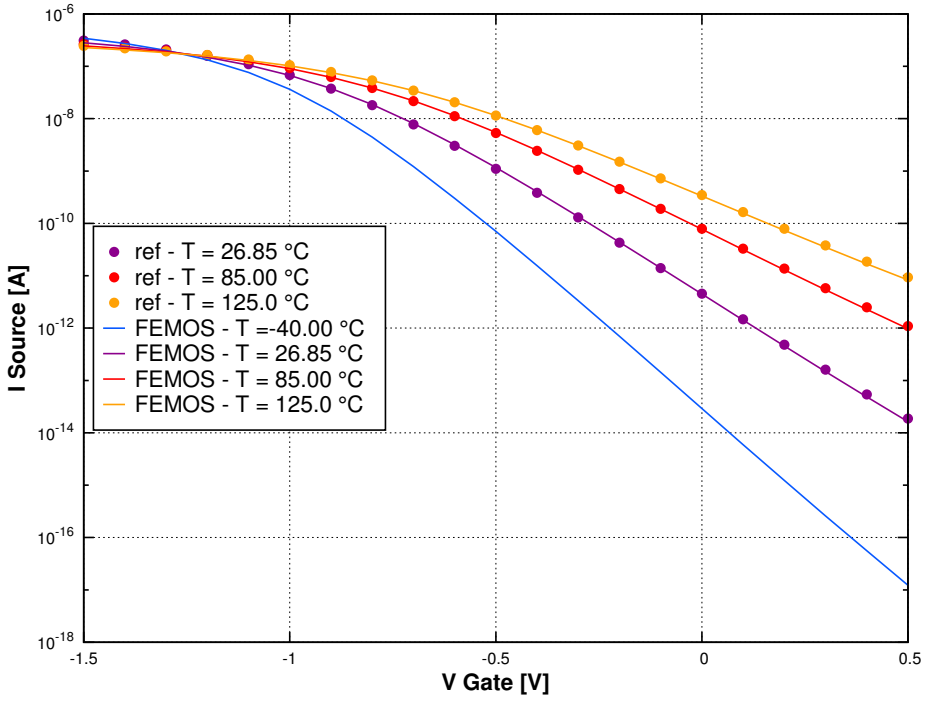

(b) p-MOSFET I_S-V_G

Figure 3.12: n-MOSFET temperature dependence analysis: comparison between FEMOS (lines) and ref. [1] (dots).

3.5 Reverse Bias

Simulations conducted in reverse bias regime represent a real numerical challenge because of the contribution of the impact ionization generation term that brings several difficulties, putting to the test the capability of the EAFE framework.

In opposition to the forward bias case, minority carriers are not mainly concentrated in the MOSFET channel but spread out in a much broader region, due to the avalanche generation phenomenon (for example in an n-channel MOSFET this happens in the so called drain end of the channel). In order to solve the associated discretized continuity equation, the simplicial partition considered must be much more refined towards the contact at which the bias is applied. On the other hand, there is no need to add degrees of freedom right next to the oxide layer, because no actual channel is present and the current flow takes place in a wider portion of the substrate.
From a theoretical standpoint, provided that the Zikatanov condition (2.29) is satisfied, we have the guarantee of the EAFE system matrix to be an M-matrix (hence ensuring the non-negativity of the solution). In practice, such condition is very unlikely to be verified for typical meshes employed in a reverse bias condition. As a consequence, the computed solution can present negative concentrations, that are not only unfeasible from a physical point of view, but being propagated to the next iteration of the Gummel map algorithm, may eventually cause the blow-up of the solution procedure.

The mesh employed for the n-MOSFETand p-MOSFET are illustrated in Fig. 3.13: the first one is noticeably more refined around the drain contact, while the second towards the source terminal. The doping is the same as in the forward bias analysis (see Fig. 3.2a and Fig. 3.2b).

Computations are performed setting all of the contacts grounded except the drain for the n-type transistor and the source for the p-type one. The R/G term is calculated switching on all the models available, hence including the band-to-band tunneling and impact ionization phenomena. As regards mobility, both the scattering from ionized impurities and the carrier velocity saturation effect are activated. The driving force (used in the Canali and Van Overstraeten- De Man models) are calculated using the gradient of the Quasi-Fermi potential.

The obtained results are quite aligned with the ones predicted by the reference tool. With respect to the n-MOSFET case (Fig. 3.14a), we can see how the two sets of current values match very well each other up until a drain bias of about 2.5 V. Afer this value of the bias voltage, a significant difference between the drain and source current is visible and the global current balance is violated (i.e., Kirchhoff's law does not hold). An inspection

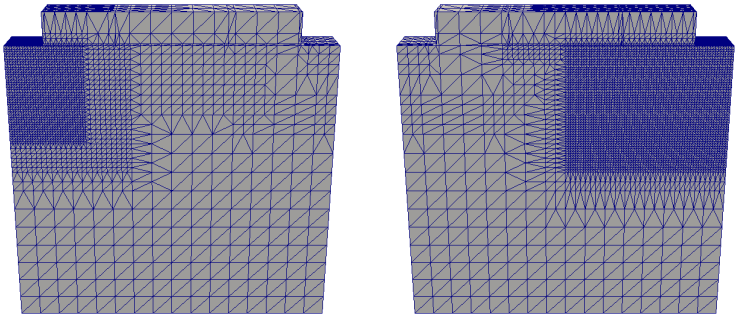

(a) *n*-MOSFET **(b)** *p*-MOSFET

Figure 3.13: Computational meshes for the reverse bias regime

V_D [V]	V_G [V]	R/G Models	Mobility Models
$0.0 \div 3.0$	0.0	SRH, Auger, Band-to-Band, Van Overstraeten - De Man	Masetti Canali (QF)

Table 3.8: *n*-MOSFET reverse bias - simulation settings

V_S [V]	V_G [V]	R/G Models	Mobility Models
$0.0 \div 2.5$	0.0	SRH, Auger, Band-to-Band, Van Overstraeten - De Man	Masetti Canali (QF)

Table 3.9: *p*-MOSFET reverse bias - simulation settings

of the electron density (Fig. 3.15) reveals the presence of zones with a negative concentration: such fact indicates the limit of the EAFE scheme, which (w.r.t. the mesh employed here) is uncapable of providing an accurate result as approaching the transistor breakdown.
The *p*-MOSFET case (Fig. 3.14b) is similar, but with some interesting differences: until an applied potential of about 1 V, all currents rapidly grow together and the main flow is from source to drain. From that point on, the bulk current overcomes in magnitude the drain current, indicating that the source current is now predominantly flowing out from the body contact. After a bias voltage of 1.3 V all values settle on a plateau which extends up to 2.0 V, thereafter, the solution algorithm is not capable of converging (w.r.t.

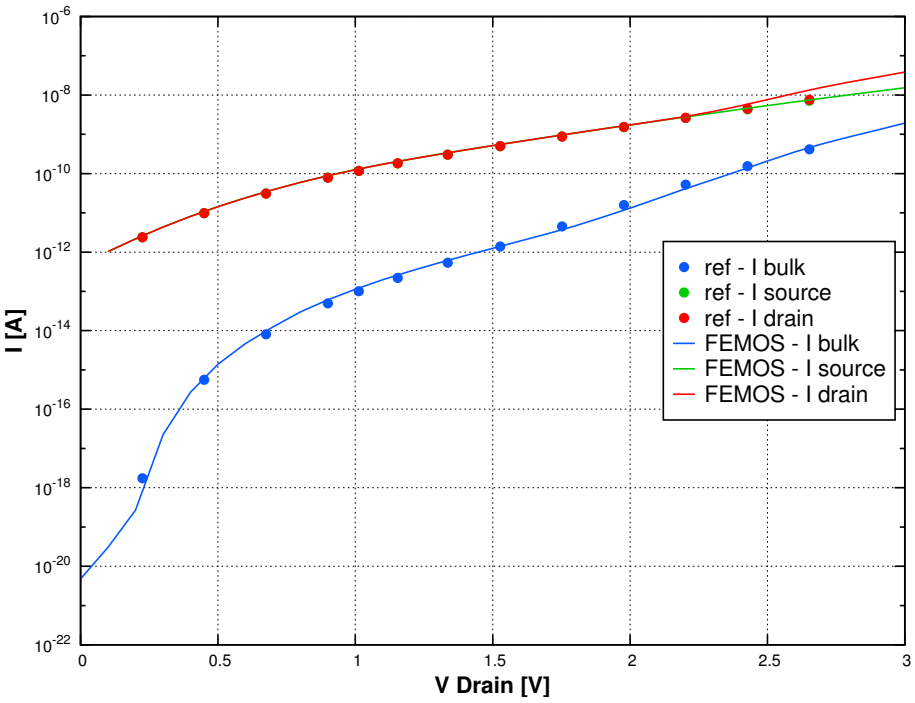

(a) *n*-MOSFET

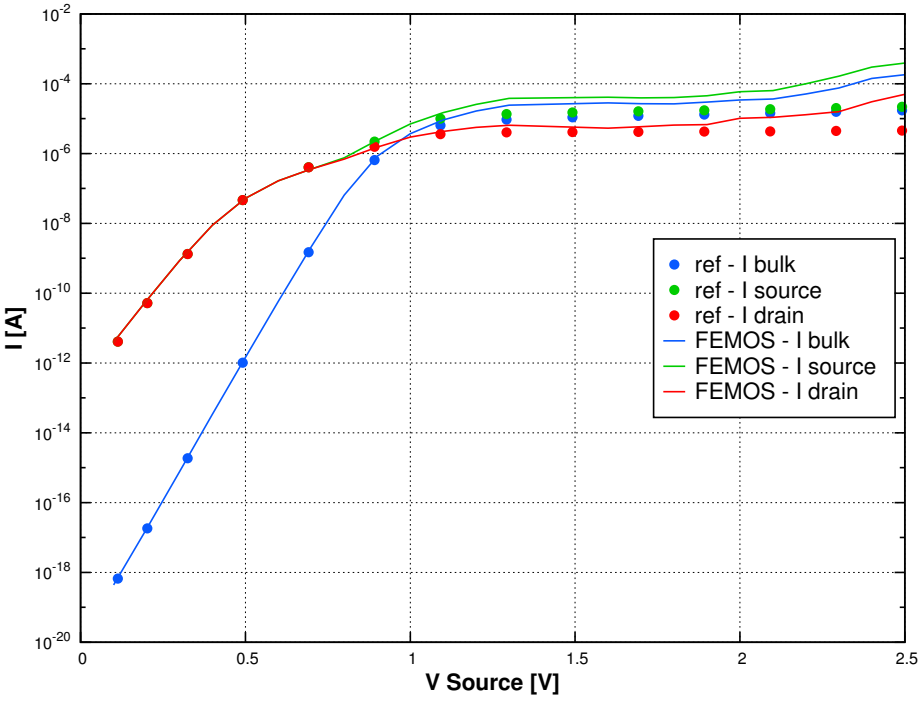

(b) *p*-MOSFET

Figure 3.14: MOSFET in reverse bias: comparison between FEMOS (lines) and Ref. [1](dots).

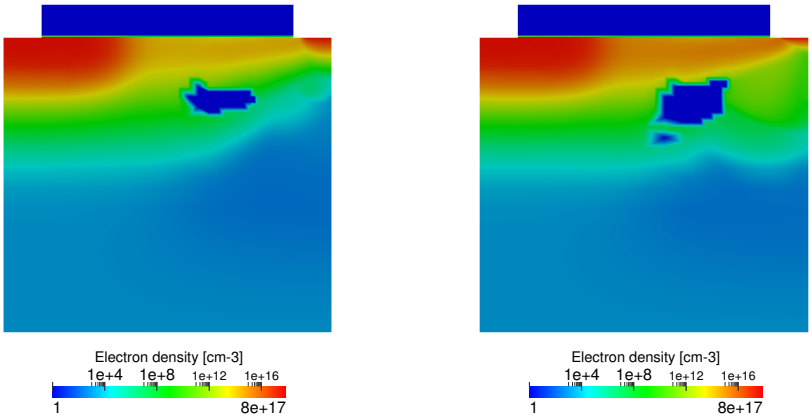

(a) $V_D = 2.0\,\mathrm{V}$ **(b)** $V_D = 3.0\,\mathrm{V}$

Figure 3.15: MOSFET in reverse bias: electron density for different drain biases.

the predefined tolerance), suggesting the occurrence of device breakdown.

For both devices, we have provided 3D snapshots of the impact ionization phenomenon in Fig. 3.16 and Fig. 3.17, where a couple of different biases have been selected for appreciating the high growth at which this quantity is subjected. All of the other R/G phenomena assume values several orders of magnitude lower, therefore making their contribution negligible in determining the conduction state of the transistor. In particular, almost no band-to band tunneling occurs, because the electric field is not enough intense (i.e., no sufficient band bending) to make it happen.
It is worth noticing that the n-type case (Fig.3.16) exhibits a generation rate which is confined in the drain region, while for p-type (Fig.3.17) both zones surrounding the source and drain terminals are interested. The cause of this discrepancy has its roots in the different paths that carriers take in the two devices. As shown in Fig.3.18a, the current density in the n-MOSFET flows in a relatively small region below the oxide layer, while in its p-channel counterpart (Fig. 3.18b), streamlines spread throughout the whole substrate due to the significantly more intense bulk current.

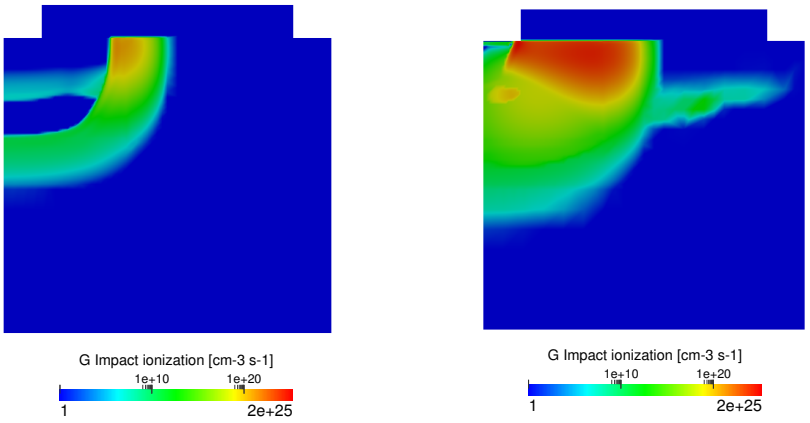

(a) $V_D = 0.5\,\mathrm{V}$ **(b)** $V_D = 2.0\,\mathrm{V}$

Figure 3.16: *n*-MOSFET in reverse bias: impact ionization rates for different drain biases.

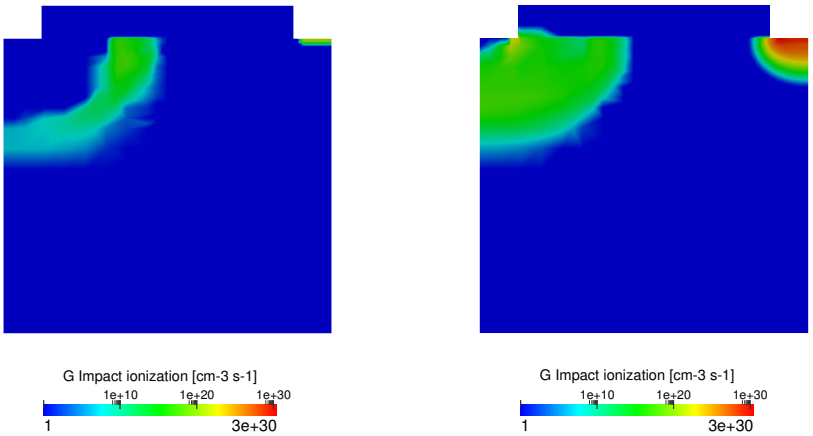

(a) $V_S = 0.5\,\mathrm{V}$ **(b)** $V_S = 1.5\,\mathrm{V}$

Figure 3.17: *p*-MOSFET in reverse bias: impact ionization rates for different source biases.

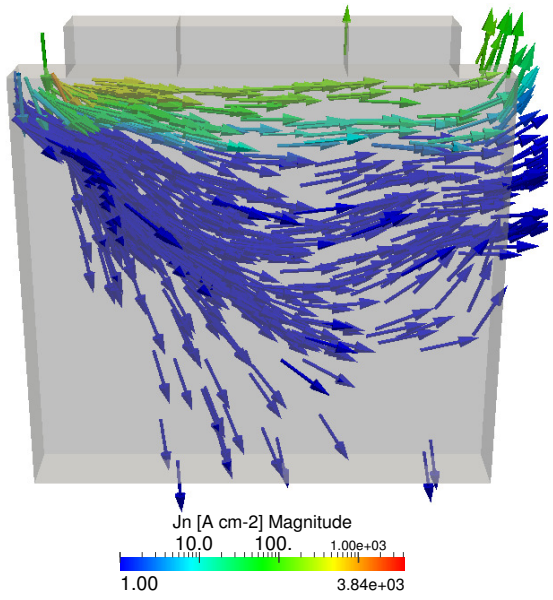

(a) *n*-MOSFET $\mathbf{J}_n$ at $V_D = 2.0\,\mathrm{V}$

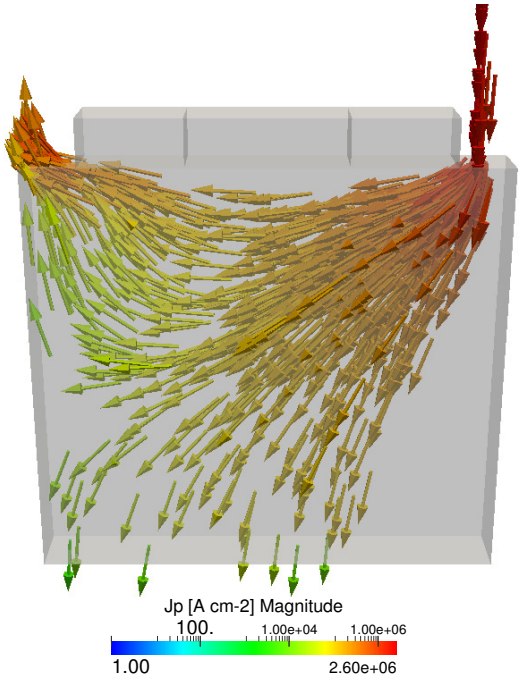

(b) *p*-MOSFET $\mathbf{J}_p$ at $V_S = 1.5\,\mathrm{V}$

Figure 3.18: MOSFET in reverse bias: current density streamlines.

Chapter 4

Transient Drift-Diffusion Model: Simulation Results

In this chapter, we present the simulation results obtained by the time dependent Drift-Diffusion model. Computations have been performed using the time discretization schemes illustrated in Sect. 2.4. The analysis is focused on the n, p MOSFET and is subdivided in two sections: in the first one, the forward bias regime has been analyzed studying the dynamic response in a variety of scenarios, while in the second one the time dependent behaviour in reverse bias conditions is addressed.

4.1 Forward Bias

In the following we consider the same n-channel and p-channel MOSFET structures employed in Chapt. 3: Fig. 3.1 reports the description of the mesh, while Fig. 3.2 illustrates the associated doping profiles.

For the sake of clarity, we briefly explain the common settings and methodology adopted in all of the time dependent simulations presented here. As regards the semiconductor physics description, we compute carrier mobilities taking into account the ionized impurities scattering and carrier velocity saturation effects, while the R/G term is given by the Shockley-Read-Hall and Auger mechanisms. The devices are supposed to be at a uniform temperature of 300 K.
The bulk contact is always assumed grounded, as well as either the source in the n-MOSFET case or the drain terminal for the p-MOSFET. All the transient simulations are obtained applying to a single contact a given pulse, as shown in Fig. 4.1: the applied pulse is a piecewise linear polynomial (in the time variable t) obtained by connecting an initial and a final value; the

four involved parameters are defined as follows:

- V_0, is the initial bias (i.e. at $t = 0$);
- V_∞, is the target/final bias;
- t_{ramp}, needed to move from V_0 to V_∞;
- T_f, is the time duration of the simulation.

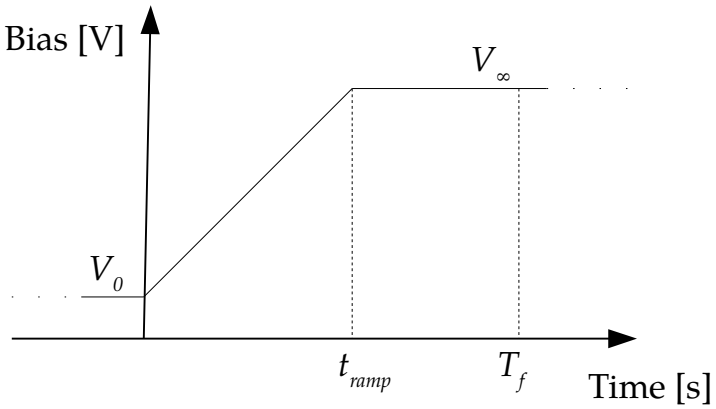

Figure 4.1: A piecewise linear pulse profile used in the transient contact

In order to prove the correctness of the implementation of the time discretization schemes, we have at first performed a few simulations to verify that current at contacts match the ones obtained by solving the associated stationary problems, when the simulation time is long enough. Both transistors have been initially set in an on-state, with 0 V drain-to-source voltage (i.e., all contacts are grounded except for the gate terminal), then, the proper contact bias (drain for the n-type, source for the p-type) has been ramped up to different target values in 1 s (see Tab. 4.1 and Tab. 4.2).

V_G [V]	$V_{D,0}$ [V]	$V_{D,\infty}$ [V]	t_{ramp} [s]	T_f [s]	Time Discr. Scheme
1.5	0.0	0.1 0.2 0.5	1	1×10^2	BE, TRBDF2

Table 4.1: n-MOSFET transient forward bias - simulation settings

V_G [V]	$V_{S,0}$ [V]	$V_{S,\infty}$ [V]	t_{ramp} [s]	T_f [s]	Time Discr. Scheme
-1.5	0.0	0.1 0.2 0.5	1	1×10^2	BE, TRBDF2

Table 4.2: p-MOSFET transient forward bias - simulation settings

For the purpose of comparing the two time discretization schemes, each simulation set-up has been run twice, one using the Backward Euler (BE) and one with the TRBDF2 method. The simulation results showed in Fig. 4.2 clearly demonstrate how the computed currents at steady-state are in well agreement with the expected value obtained with the stationary approach for source and drain contacts.

We report the carrier densities obtained with the BE or TRBDF2 method and those associated with the steady-state simulations in Fig. 4.3 for the n-MOSFET and Fig. 4.4 for the p-MOSFET: the results are indistinguishable.

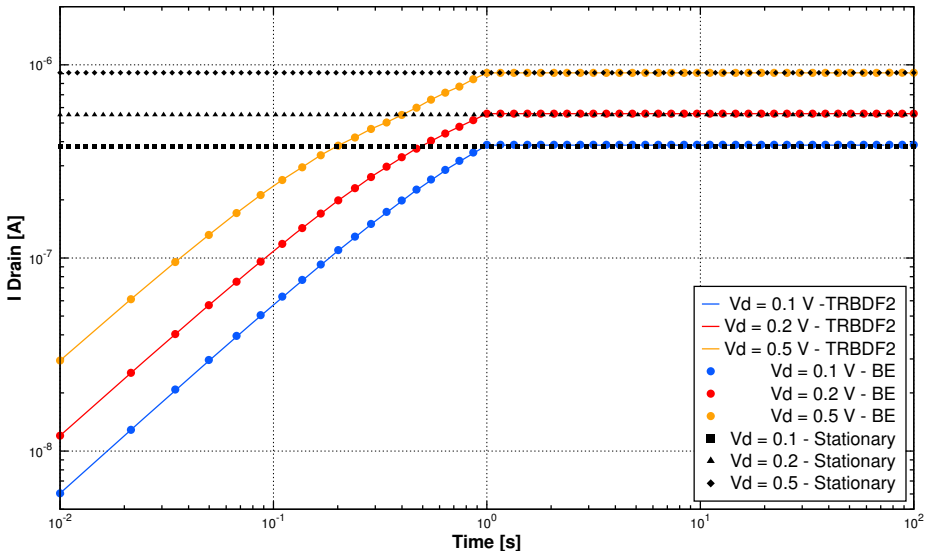

(a) n-MOSFET - drain current for different values of $V_{D,\infty}$

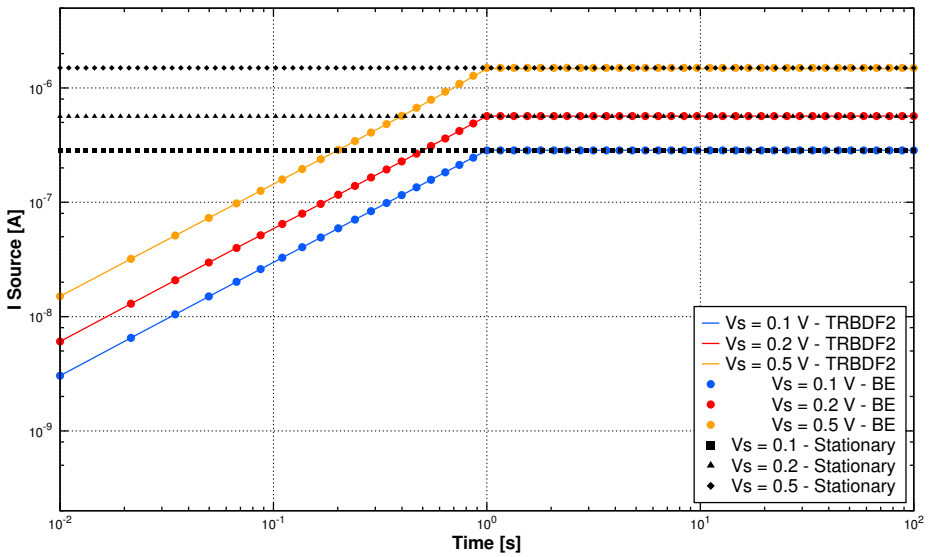

(b) p-MOSFET - source current for different values of $V_{S,\infty}$

Figure 4.2: Transient simulations in forward bias: comparison between asymptotic and stationary results in different bias conditions and for different time discretization schemes.

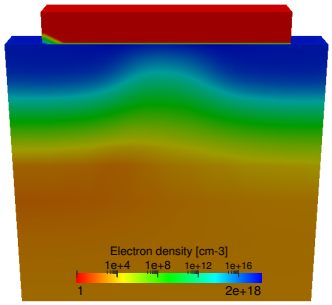

(a) BE, $T = T_f$

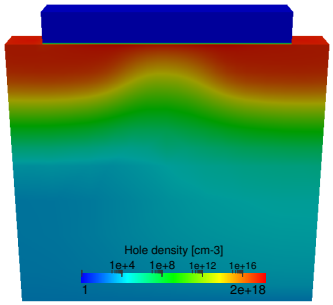

(a) BE, $T = T_f$

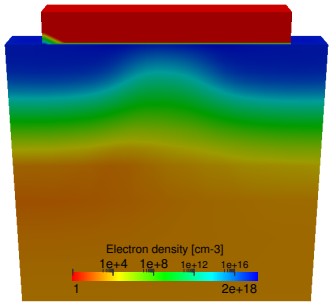

(b) TRBDF2, $T = T_f$

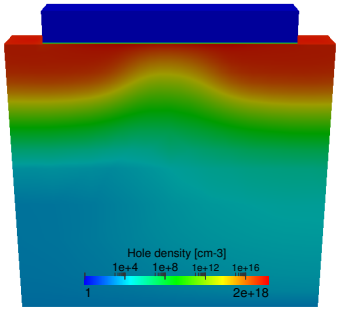

(b) TRBDF2, $T = T_f$

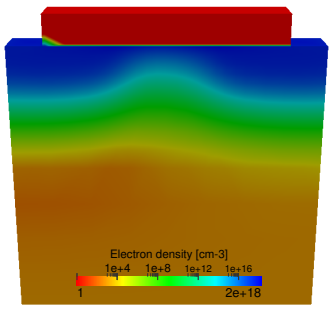

(c) Stationary

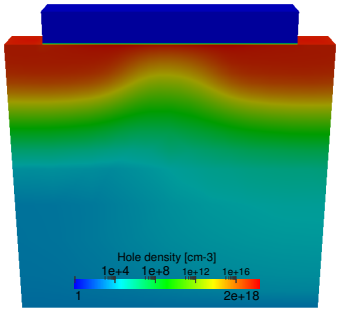

(c) Stationary

Figure 4.3: n-MOSFET transient simulations in forward bias: comparison between asymptotic and stationary electron density distributions at $V_D = 0.1$ V and $V_G = 1.5$ V

Figure 4.4: p-MOSFET transient simulations in forward bias: comparison between asymptotic and stationary hole density distributions at $V_S = 0.1$ V and $V_G = -1.5$ V

We have pursued the transient analysis studying the device dynamic response in further scenarios using only the BE method:

- **gate step**, starting from an off-state and a non zero drain-to-source applied bias, the transistors are rapidly switched in the on-state;
- **gate backward facing step**, starting from an on-state and a non zero drain-to-source applied bias, the transistors are rapidly switched off;
- **drain/source step**, starting from an on-state and a zero drain-to-source applied bias, either the drain (n-MOSFET) or source (p-MOSFET) potential is rapidly increased to a target value;
- **drain/source backward facing step**, starting from an on-state and a non zero drain-to-source applied bias, either the drain (n-MOSFET) or source (p-MOSFET) potential is rapidly decreased to zero.

The results are presented in Figs. 4.5–4.8 together with the associated settings, which are summarized in Tabs. 4.3–4.10: the computed values are always in good agreement with the outputs of the corresponding stationary problems, except for the source/drain backward facing step (Fig. 4.8), where both the drain and source currents tend to vanish but still have a higher value than their steady counterpart.

It is interesting to notice the behaviour in the n-MOSFET in both the gate switch on and off simulations: a discrepancy between source and drain currents is present in the first case with the fastest ramp time (Fig. 4.6a), while is less evident, but still present, in the second case (Fig. 4.5a). The reason is related to the time needed for holes to flow in/out to/from the p-substrate due to their mobility which is far lower than that of electrons. In the p-MOSFET, the majority carriers in the substrate are electrons which, thanks to their higher mobility, respond more rapidly to voltage variations.

From a computational perspective, we point out how the drain/source switch off simulations are the more expensive: as shown in Fig. 4.8a-b, the high number of timesteps required is evident.

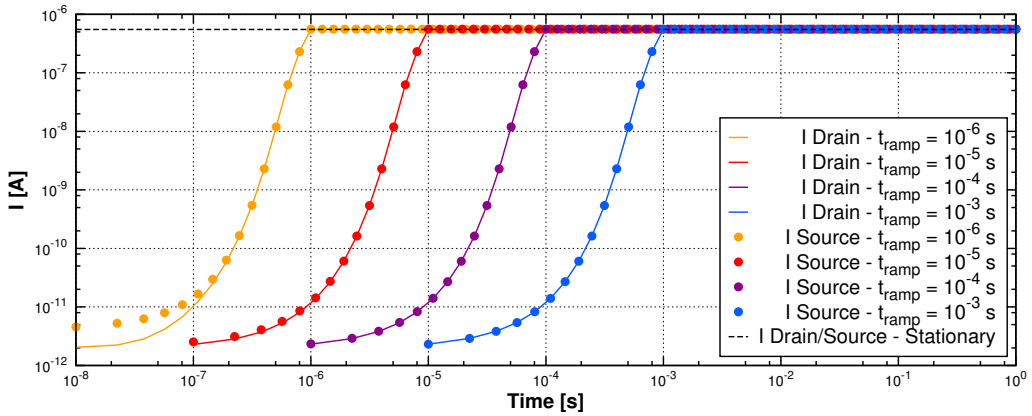

(a) n-MOSFET

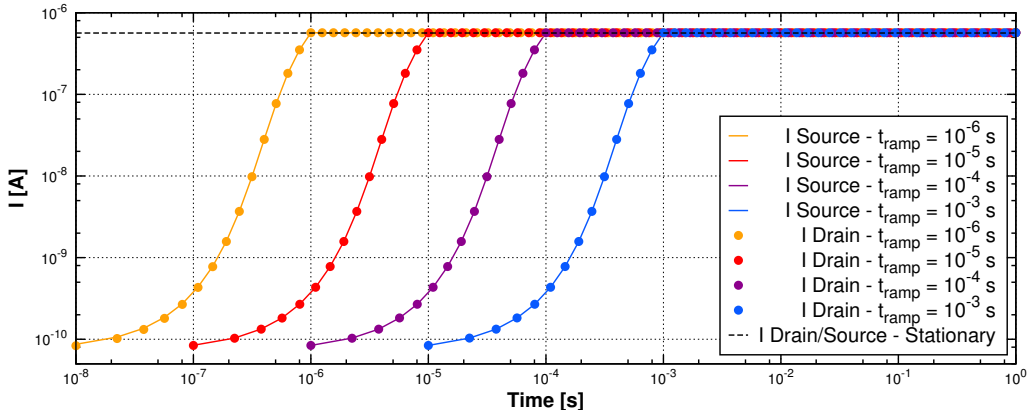

(b) p-MOSFET

Figure 4.5: Gate step transient simulations: drain and source currents for different values of t_{ramp}

V_D [V]	$V_{G,0}$ [V]	$V_{G,\infty}$ [V]	t_{ramp} [s]	T_f [s]	Time Discr. Scheme
0.2	0.0	1.5	1×10^{-3}, 1×10^{-4}, 1×10^{-5}, 1×10^{-6}	1	BE

Table 4.3: n-MOSFET gate step - simulation settings

V_S [V]	$V_{G,0}$ [V]	$V_{G,\infty}$ [V]	t_{ramp} [s]	T_f [s]	Time Discr. Scheme
0.2	0.0	-1.5	1×10^{-3}, 1×10^{-4}, 1×10^{-5}, 1×10^{-6}	1	BE

Table 4.4: p-MOSFET gate step - simulations settings

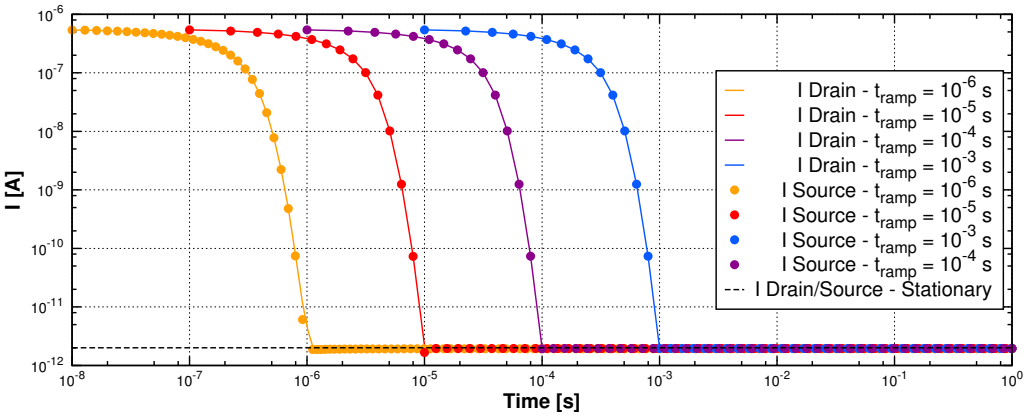

(a) n-MOSFET

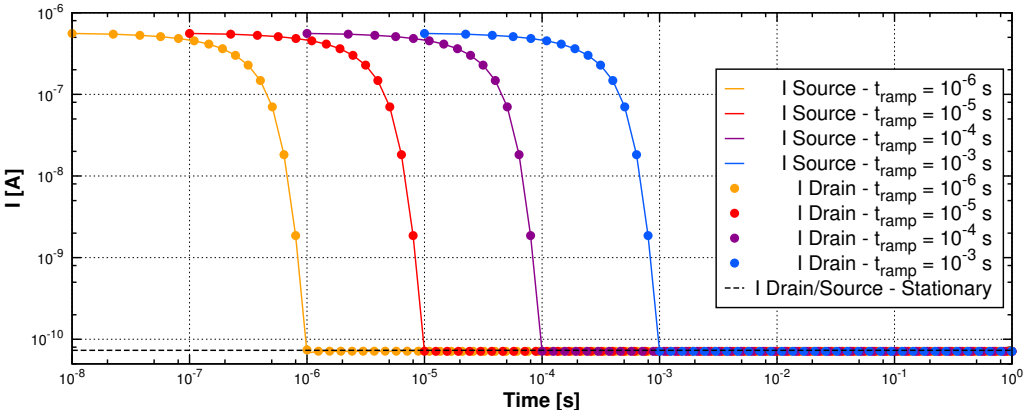

(b) p-MOSFET

Figure 4.6: Gate backward facing step transient simulations: drain and source currents for different values of t_{ramp}

V_D [V]	$V_{G,0}$ [V]	$V_{G,\infty}$ [V]	t_{ramp} [s]	T_f [s]	Time Discr. Scheme
0.2	0.0	1.5	1×10^{-3}, 1×10^{-4}, 1×10^{-5}, 1×10^{-6}	1	BE

Table 4.5: n-MOSFET gate backward step - simulation settings

V_S [V]	$V_{G,0}$ [V]	$V_{G,\infty}$ [V]	t_{ramp} [s]	T_f [s]	Time Discr. Scheme
0.2	-1.5	0.0	1×10^{-3}, 1×10^{-4}, 1×10^{-5}, 1×10^{-6}	1	BE

Table 4.6: p-MOSFET gate backward step - simulation settings

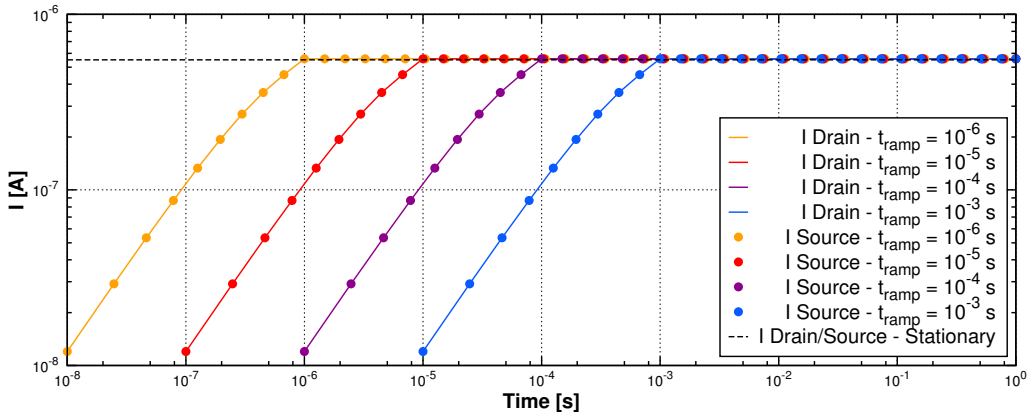

(a) n-MOSFET

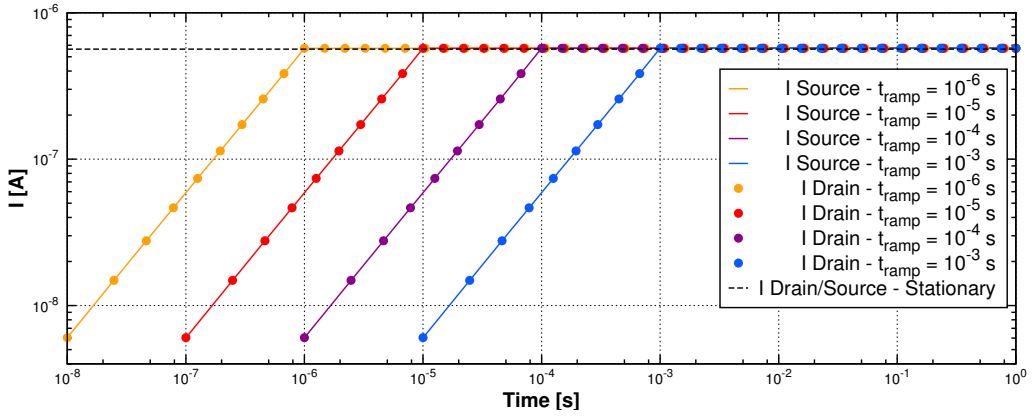

(b) p-MOSFET

Figure 4.7: Drain step transient simulations: drain and source currents for different values of t_{ramp}

V_G [V]	$V_{D,0}$ [V]	$V_{D,\infty}$ [V]	t_{ramp} [s]	T_f [s]	Time Discr. Scheme
1.5	0.0	0.2	1×10^{-3}, 1×10^{-4}, 1×10^{-5}, 1×10^{-6}	1	BE

Table 4.7: n-MOSFET drain step - simulation settings

V_G [V]	$V_{S,0}$ [V]	$V_{S,\infty}$ [V]	t_{ramp} [s]	T_f [s]	Time Discr. Scheme
-1.5	0.0	0.2	1×10^{-3}, 1×10^{-4}, 1×10^{-5}, 1×10^{-6}	1	BE

Table 4.8: p-MOSFET source step - simulation settings

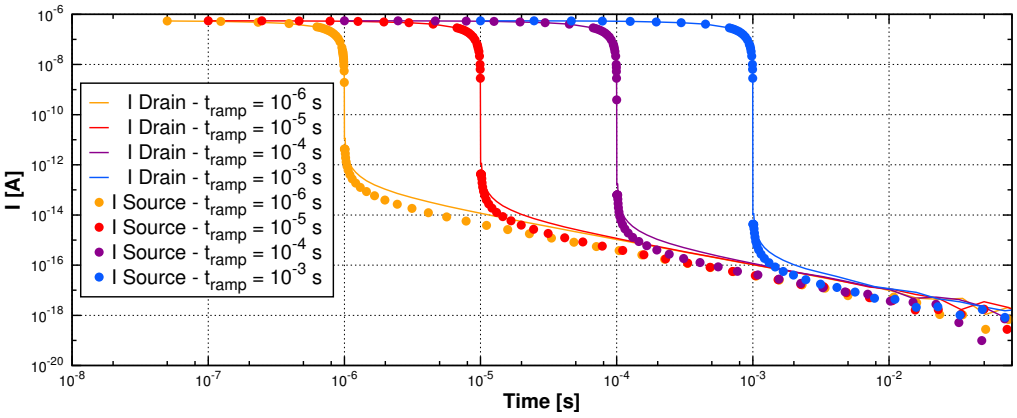

(a) n-MOSFET

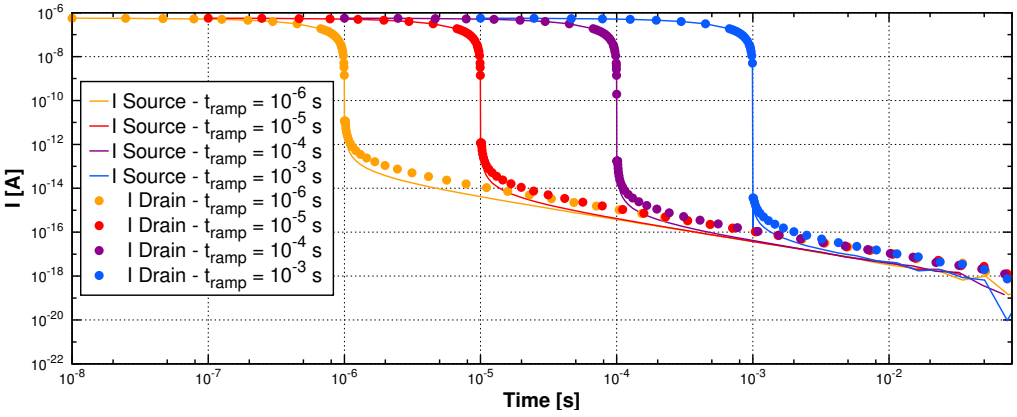

(b) p-MOSFET

Figure 4.8: Drain backward facing step transient simulations: drain and source currents for different values of t_{ramp}

V_G [V]	$V_{D,0}$ [V]	$V_{D,\infty}$ [V]	t_{ramp} [s]	T_f [s]	Time Discr. Scheme
1.5	0.2	0.0	1×10^{-3}, 1×10^{-4}, 1×10^{-5}, 1×10^{-6}	1	BE

Table 4.9: n-MOSFET drain backward step - simulation settings

V_G [V]	$V_{S,0}$ [V]	$V_{S,\infty}$ [V]	t_{ramp} [s]	T_f [s]	Time Discr. Scheme
-1.5	0.2	0.0	1×10^{-3}, 1×10^{-4}, 1×10^{-5}, 1×10^{-6}	1	BE

Table 4.10: p-MOSFET source backward step - simulation settings

4.2 Reverse Bias

In order to perform a meaningful comparison in reverse bias conditions, the mesh and doping profiles of the MOSFET structures are the same as in the steady-state case (Sect. 3.5, Fig. 3.13 and Fig. 3.2). The considered physical phenomena are the ionized impurity scattering and the carrier velocity saturation, while the R/G term is computed by activating all of the implemented models (see Tab. 4.11).

R/G Models	Mobility Models	Driving Force
SRH, Auger, Band-to-Band, Van Overstraeten - De Man	Masetti Canali	Gradient of quasi Fermi potential

Table 4.11: Transient reverse bias - physical phenomena considered for both MOSFETs

Simulations have been performed as follows: for both trasistors all contacts are initially grounded, then the drain (n-MOSFET) or source (p-MOSFET) bias has been raised to a target value. The choice of the time discretization scheme has fallen upon the TRBDF2 method due to its higher convergence rate. All of the temporal settings are summarized in Tab. 4.12 and Tab. 4.13.

Results for the n-MOSFET and p-MOSFET are provided in Fig. 4.9 and Fig. 4.10, respectively: the agreement with the steady-state values is evident once the transient is estinguished.

In Figs. 4.11–4.16 we report the asymptotic and stationary 3D representations of the impact ionization generation term, the electric field and the minority carrier current densities for both devices: in all cases, the computed profiles coincede without any appreciable difference.

$V_{D,0}$ [V]	$V_{D,\infty}$ [V]	t_{ramp} [s]	T_f [s]	Time Discr. Scheme
0.0	1.0	1.0×10^{-3}	1×10^{-1}	TRBDF2
	1.5	1.5×10^{-3}		
	2.0	2.0×10^{-3}		

Table 4.12: p-MOSFET transient reverse bias - simulation settings

$V_{S,0}$ [V]	$V_{S,\infty}$ [V]	t_{ramp} [s]	T_f [s]	Time Discr. Scheme
0.0	1.0	0.5×10^{-3}	1×10^{-1}	TRBDF2
	1.5	0.75×10^{-3}		
	2.0	1.0×10^{-3}		

Table 4.13: p-MOSFET transient reverse bias - simulation settings

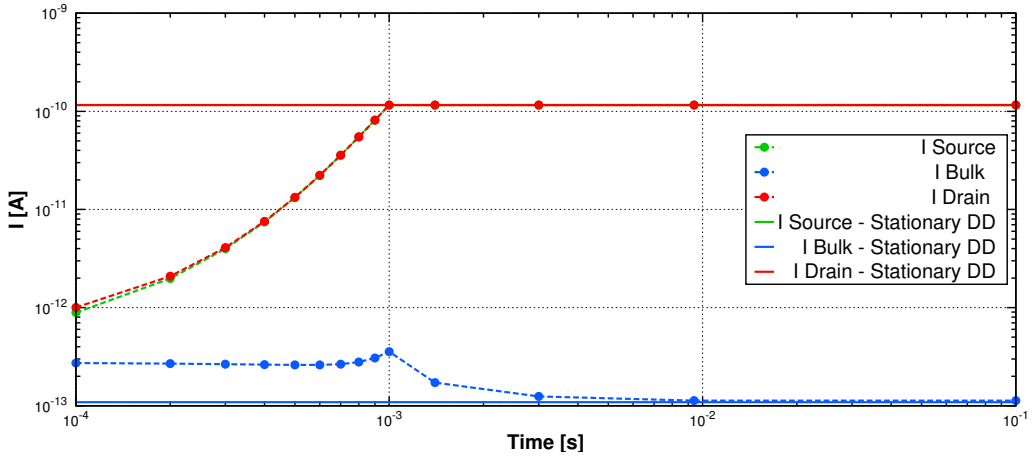

(a) $V_{D,\infty} = 1.0$ V

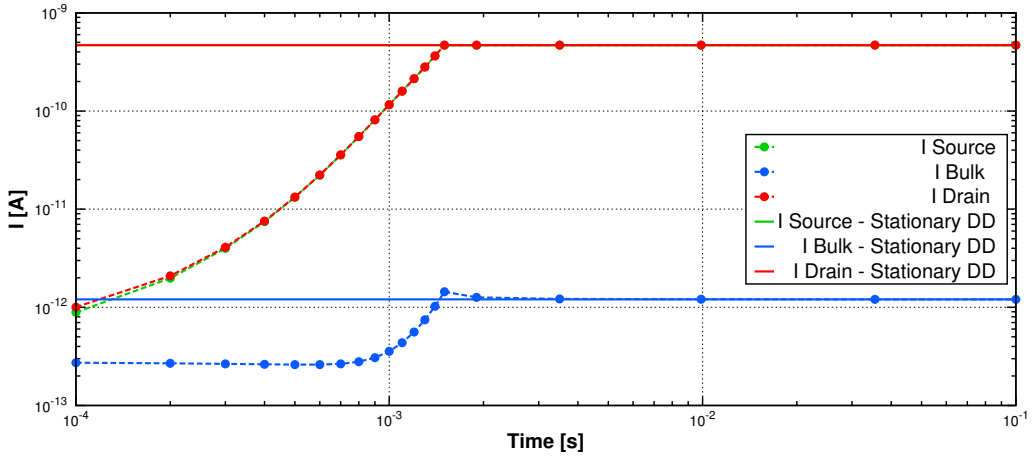

(b) $V_{D,\infty} = 1.5$ V

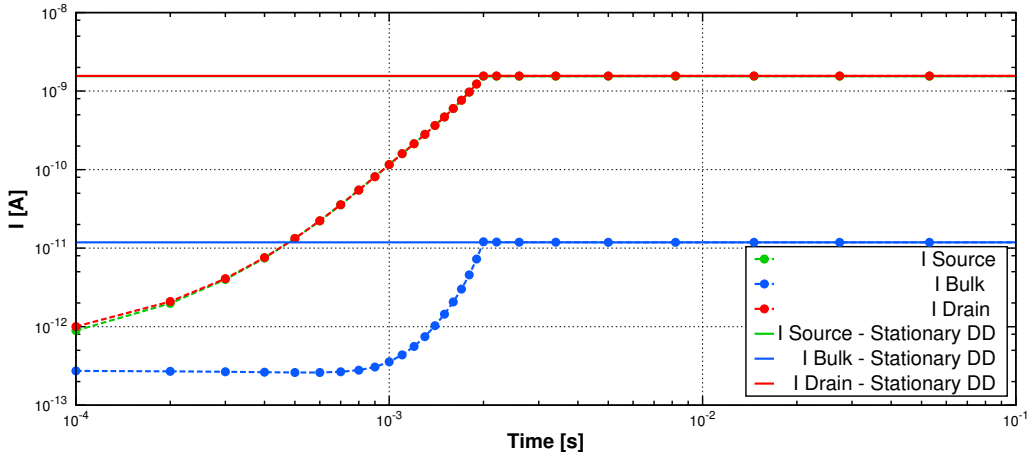

(c) $V_{D,\infty} = 2.0$ V

Figure 4.9: n-MOSFET transient simulations in reverse bias: comparison between asymptotic and stationary results for different values of $V_{D,\infty}$.

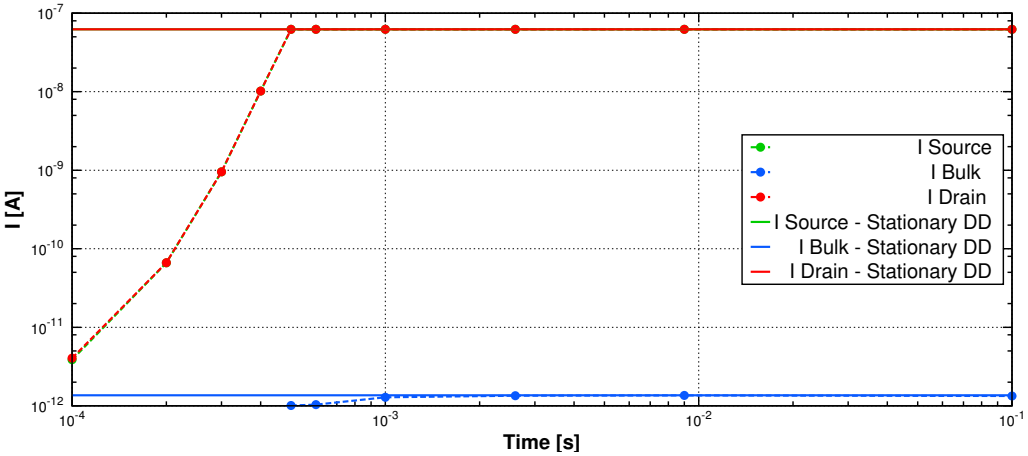

(a) $V_{S,\infty} = 0.5$ V

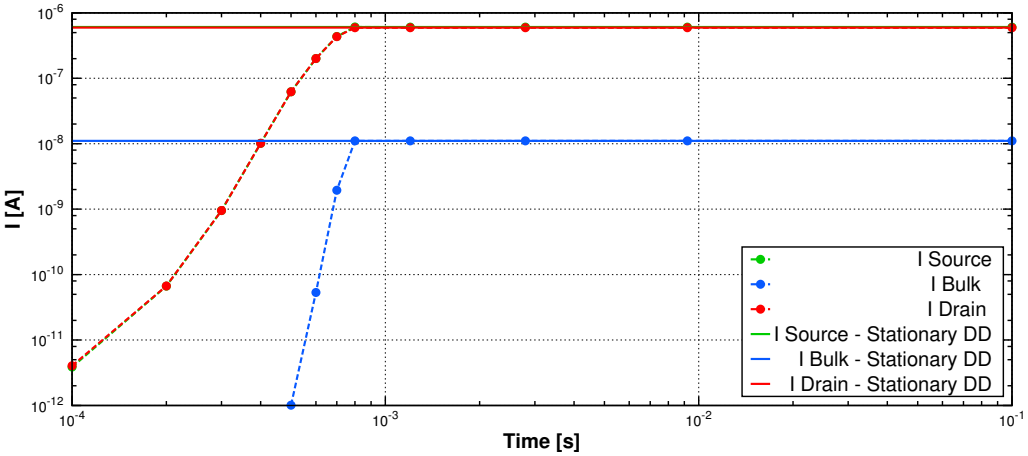

(b) $V_{S,\infty} = 0.75$ V

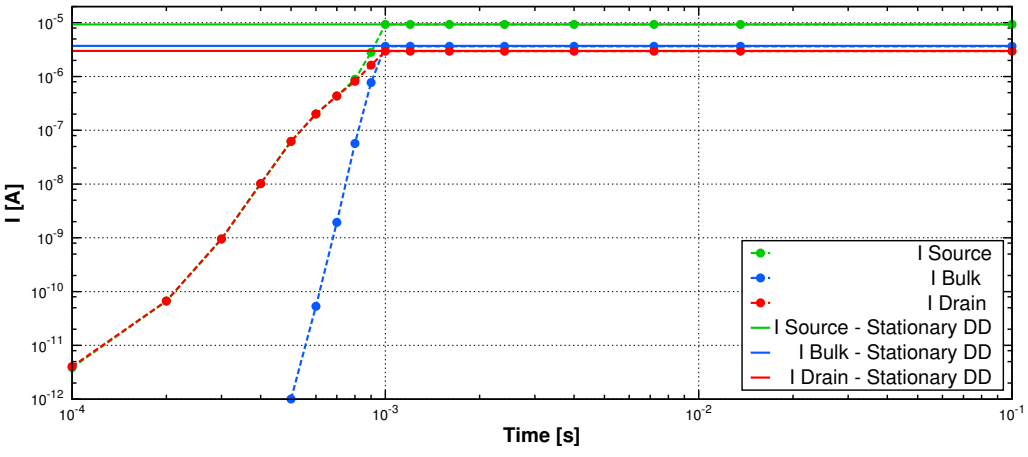

(c) $V_{S,\infty} = 1.0$ V

Figure 4.10: p-MOSFET transient simulations in reverse bias: comparison between asymptotic and stationary results for different values of $V_{S,\infty}$.

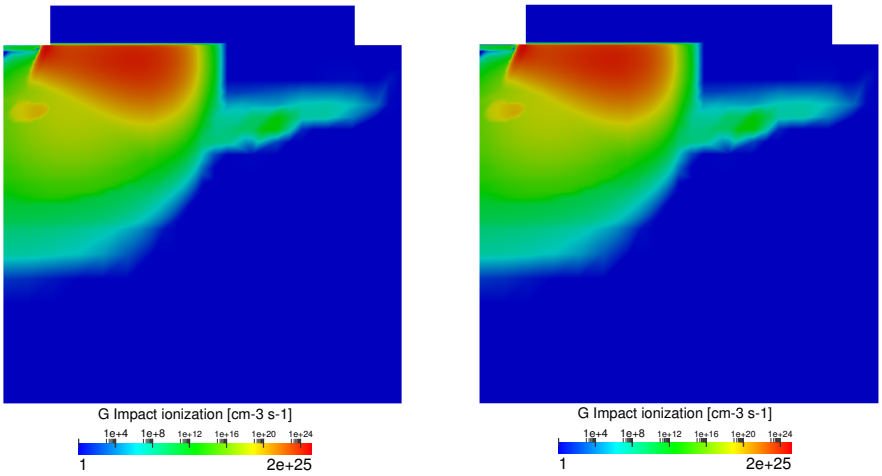

(a) $t = T_f$ **(b)** Stationary

Figure 4.11: n-MOSFET transient simulations in reverse bias: comparison between asymptotic and stationary impact ionization generation terms at $V_D = 2.0$ V

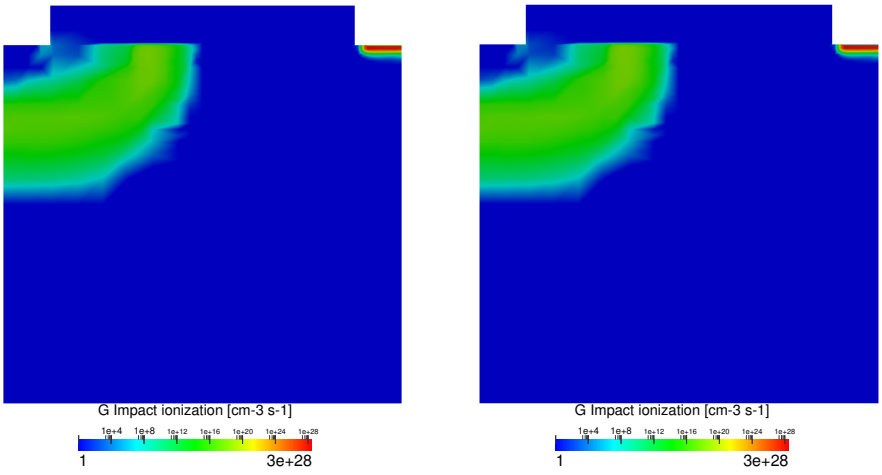

(a) $t = T_f$ **(b)** Stationary

Figure 4.12: p-MOSFET transient simulations in reverse bias: comparison between asymptotic and stationary impact ionization generation terms at $V_S = 1.0$ V

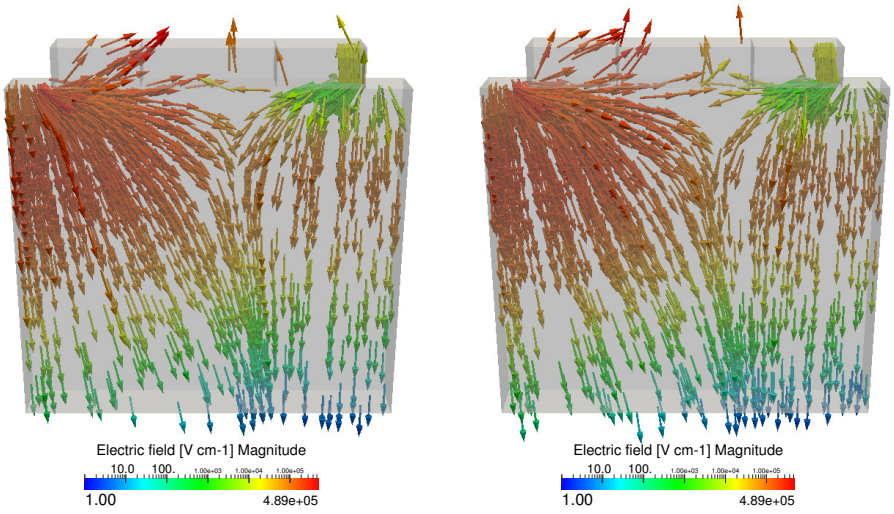

(a) $t = T_f$ **(b)** Stationary

Figure 4.13: n-MOSFET transient simulations in reverse bias: comparison between asymptotic and stationary electric field profiles at $V_D = 2.0$ V

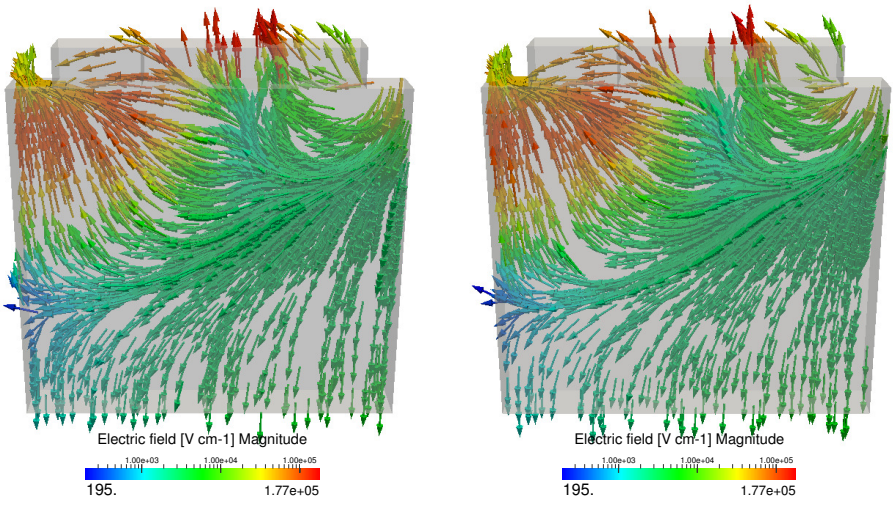

(a) $t = T_f$ **(b)** Stationary

Figure 4.14: p-MOSFET transient simulations in reverse bias: comparison between asymptotic and stationary electric field profiles at $V_S = 1.0$ V

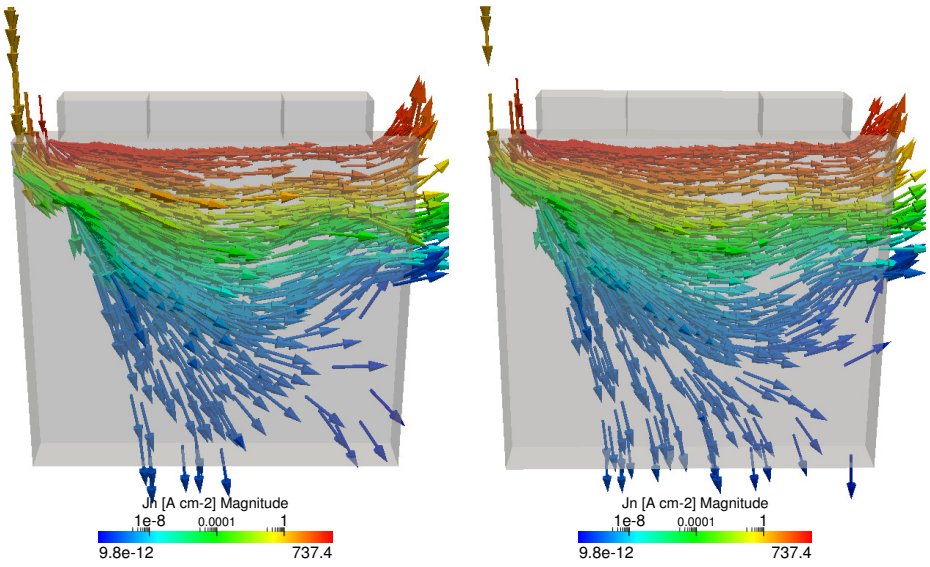

(a) $t = T_f$ **(b)** Stationary

Figure 4.15: n-MOSFET transient simulations in reverse bias: comparison between asymptotic and stationary electron current densities at $V_D = 2.0$ V

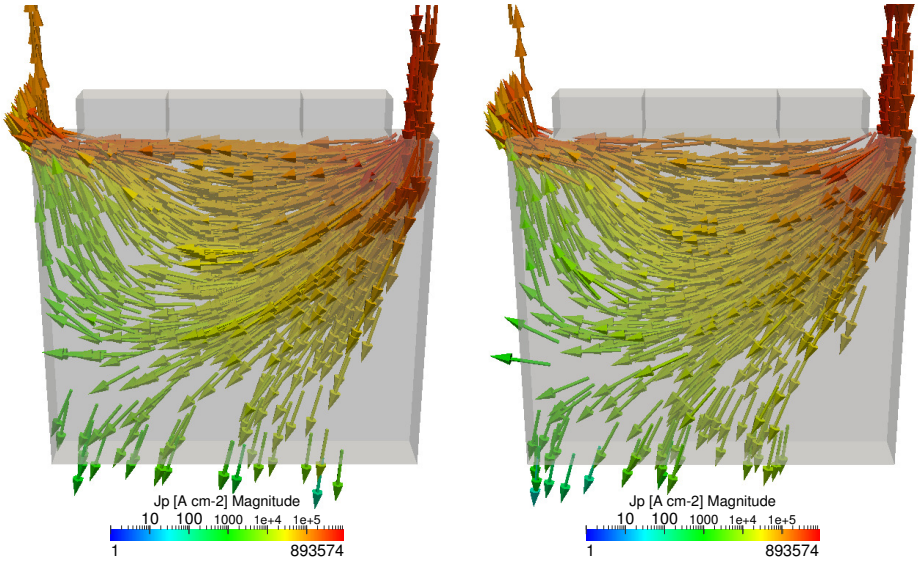

(a) $t = T_f$ **(b)** Stationary

Figure 4.16: p-MOSFET transient simulations in reverse bias: comparison between asymptotic and stationary hole current densities at $V_S = 1.0$ V

Chapter 5

Conclusions and Future Works

In this thesis we have dealt with the simulation of 3D semiconductor devices by extending the FEMOS-MP computer code in order to improve perfomance, flexibility and functionality of the dedicated modules. These coding efforts have made it possible:

- to include models of new physical phenomena, such as the band-to-band tunneling, the bandgap narrowing and the mobility degradation induced by the electric field;
- to perform transient simulations using either the Backward Euler or the TRBDF2 time discretization schemes;
- to perform simulations at different uniform temperatures.

The correctness of the implementation has been thoroughly tested in a wide variety of scenarios, exhibiting a very good agreement with the reference commercial software for stationary simulations and being self-consistent with the steady-state results in the transient analysis.

Future activities will be devoted to the following objectives:

- the coupling of the Drift-Diffusion equation system with a proper thermal model;
- the development of the doping profile setting with meshes generated by `Gmsh` [1].

[1] `http://gmsh.info`

Bibliografia

[1] *Sentaurus Device User Guide*. Synopsis Inc., 2013.

[2] R. E. Bank, W. M. Coughran, W. Fichtner, E. H. Grosse, D. J. Rose, and R. K. Smith. Transient simulation of silicon devices and circuits. *IEEE Transactions on Computer-Aided Design*, 4:436–451, 1985.

[3] A. Bortolossi. 3d finite element drift-diffusion simulation of semiconductor devices. Master's thesis, Politecnico di Milano, 2014.

[4] C. Canali. Electron and hole drift velocity measurements in silicon and their empirical relation to electric field and temperature. *IEEE Transactions on Electron Devices*, 22:1045–1047, 1975.

[5] A. G. Chynoweth. Ionization rates for electrons and holes in silicon. *Physical Review*, 109:1537–1540, 1958.

[6] P. Deuflhard. A modified newton method for the solution of ill-conditioned system of nonlinear equations with application to multiple shooting. *Numer. Math*, 22:289–315, 1974.

[7] H. K. Gummel. A self-consistent iterative scheme for one-dimensional steady state transistor calculations. *Electron Devices*, pages 455–465, 1964.

[8] H. K. Gummel and D. Scharfetter. Large-signal analysis of a silicon read diode oscillator. *IEEE Trans. Electron Devices*, pages 64–77, 1969.

[9] J. D. Jackson. *Elettrodinamica Classica*. Zanichelli, 1984.

[10] J. W. Jerome. *Analysis of Charge Transport*. Springer, 1996.

[11] C. Lombardi. A physically based mobility model for numerical simulation of nonplanar devices. *IEEE Transactions on Computer-Aided Design*, 7:1164–1171, 1988.

[12] P.A. Markowich, C.A. Ringhofer, and Schmeiser C. *Semiconductor Equations*. Springer, 1990.

[13] G. Masetti and M. Severi. Modeling of carrier mobility against carrier concentration in arsenic-, phosphorus-, and boron-doped silicon. *IEEE Transactions on Electron Devices*, 7:764–769, 1983.

[14] A. Mauri, A. Bortolossi, G. Novielli, and R. Sacco. 3d finite element modeling and simulation of industrial devices including impact ionization. *Mathematics in Industry*, 5, 2015.

[15] A. Quarteroni. *Numerical Models for Differential Problems*. Springer, 2008.

[16] S. Salsa. *Equazioni a Derivate Parziali, metodi, modelli e applicazioni*. Springer Italia, Milan, 2010.

[17] A. Schenk. Rigorous theory and simplified model of the band-to-band tunneling in silicon. *Solid-State Electronics*, 36(1):19—-34, 1993.

[18] S. Selberherr. *Analysis and Simulation of Semiconductor Devices*. Springer, 1984.

[19] R. van Overstraeten and H. de Man. Measurement of the ionization rates in diffused silicon p-n junctions. *Solid-State Electronics*, 13:583–608, 1970.

[20] Y. P. Varshni. Temperature dependence of the energy gap in semiconductors. *Physica*, 34(1):149–154, 1967.

[21] J. Xu and L.T. Zikatanov. A monotone finite element scheme for convection-diffusion equations. *Mathematics of Computation*, 68:1429–1446, 1999.

[22] T. Yuan and H. N. Tak. *Fundamentals of Modern VLSI Devices*. Cambridge University Press, 2009.

[23] L. T. Zikatanov and R. D. Lazarov. An exponential fitting scheme for general convection-diffusion equations on tetrahedral meshes. *Computational and Applied Mathematics*, 1:60–69, 2012.

Ringraziamenti

Desidero ringraziare Aurelio e il prof. Sacco per avermi seguito e aiutato a realizzare questo lavoro e, cosa che reputo più importante, per la comprensione e la gentilezza dimostrata in questo periodo difficile.

Ringrazio la mia meravigliosa famiglia: mamma, papà e Clelia grazie per avermi supportato e sopportato tutti questi anni, non so se riuscirò mai a farvi capire quanto vi sono grato. Rimnanendo in famiglia, un ringraziamento speciale va a voi, Anna e Rita.

Ringrazio tutti i miei fantastici amici, della piazza e non, che non nominerò per ragioni di spazio e per evitare la figuraccia di averne dimenticato qualcuno (come succede di solito): pagherò pegno offrendovi da bere. L'unico strappo alla regola è per te, Dela: non posso più offrirti nulla, ma i tuoi meriti sono grandi almeno quanto lo eri tu, gigante.

Infine, un doveroso ringraziamento va a tutti i professori che ho incontrato nel corso della mia carriera scolastica, in particolare durante gli splendidi anni passati all'ITIS: se sono qui lo devo senz'altro anche a voi.

La lista di tutte le persone che vorrei ringraziare è ovviamente molto più lunga, ma la speranza è che non serva menzionarle in questa pagina affinché sappiano quanto io sia loro riconoscente.